Cell

Resource

Spatial proteomics in three-dimensional intact specimens

Graphical abstract

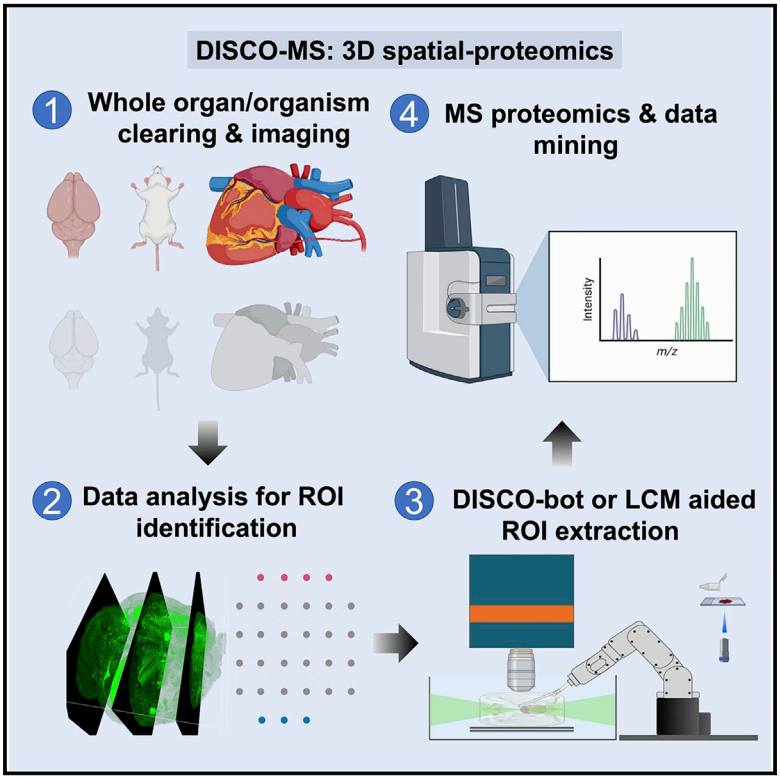

Authors

Harsharan Singh Bhatia, Andreas-David Brunner, Furkan Öztürk, ..., Fabian Theis, Matthias Mann, Ali Ertürk

Correspondence

mmann@biochem.mpg.de (M.M.), erturk@helmholtz-muenchen.de (A.E.)

In brief

DISCO-MS and DISCO-bot allows for unbiased spatial proteome analysis of small tissue regions identified by panoptic imaging of large cleared samples, *in silico* reconstructions, and automated minimally invasive robotic tissue extraction.

Highlights

- DISCO-MS is a spatial proteomics technology in optically cleared whole specimens
- DISCO-MS is aided by AI and robotics and yields proteome similar to fresh samples
- DISCO-bot-aided DISCO-MS reveals spatial immune cell heterogeneity in mouse bones
- DISCO-bot-aided DISCO-MS reveals plaque heterogeneity in human coronary artery

Bhatia et al., 2022, Cell *185*, 5040–5058
December 22, 2022
https://doi.org/10.1016/j.cell.2022.11.021

CellPress

CellPress

Cell

Resource

Spatial proteomics in three-dimensional intact specimens

Harsharan Singh Bhatia,[1,2,24] Andreas-David Brunner,[3,4,24] Furkan Öztürk,[1,24] Saketh Kapoor,[1] Zhouyi Rong,[1,2,13] Hongcheng Mai,[1,2,13] Marvin Thielert,[3] Mayar Ali,[1,5] Rami Al-Maskari,[2,7,8] Johannes Christian Paetzold,[1,7,8,10] Florian Kofler,[7,8,9,12] Mihail Ivilinov Todorov,[1,2] Muge Molbay,[1,2,13] Zeynep Ilgin Kolabas,[1,2,5] Moritz Negwer,[1] Luciano Hoeher,[1] Hanno Steinke,[19] Alina Dima,[7,8] Basavdatta Gupta,[1] Doris Kaltenecker,[2,14] Özüm Sehnaz Caliskan,[15,16] Daniel Brandt,[15,16] Natalie Krahmer,[15,16] Stephan Müller,[17,18] Stefan Frieder Lichtenthaler,[5,6,17,18] Farida Hellal,[1,2] Ingo Bechmann,[19] Bjoern Menze,[7,8,11] Fabian Theis,[20,21,22] Matthias Mann,[3,23,*] and Ali Ertürk[1,2,5,6,25,*]

[1]Insititute for Tissue Engineering and Regenerative Medicine (iTERM), Helmholtz Zentrum München, 85764 Neuherberg, Germany
[2]Institute for Stroke and Dementia Research, Klinikum der Universität München, Ludwig-Maximilians University Munich, 81377 Munich, Germany
[3]Department for Proteomics and Signal Transduction, Max Planck Institute of Biochemistry, 82152 Martinsried, Germany
[4]Boehringer Ingelheim Pharma GmbH & Co. KG, Drug Discovery Sciences, Birkendorfer Str. 65, D-88400 Biberach Riss, Germany
[5]Graduate School of Neuroscience (GSN), 82152 Munich, Germany
[6]Munich Cluster for Systems Neurology (SyNergy), 81377 Munich, Germany
[7]Center for Translational Cancer Research (TranslaTUM) of the TUM, 81675 Munich, Germany
[8]Image-Based Biomedical Modeling, Department of Informatics, Technical University of Munich, 85748 Garching, Germany
[9]Helmholtz AI, Helmholtz Zentrum München, 85764 Neuherberg, Germany
[10]Biomedical Image Analysis Group, Department of Computing, Imperial College London, London SW7 2AZ, UK
[11]Department for Quantitative Biomedicine, University of Zurich, 8006 Zurich, Switzerland
[12]Department of Neuroradiology, Klinikum rechts der Isar, 81675 Munich, Germany
[13]Munich Medical Research School (MMRS), 80336 Munich, Germany
[14]Institute for Diabetes and Cancer, Helmholz Zentrum München, 85764 Neuherberg, Germany
[15]Institute for Diabetes and Obesity, Helmholz Zentrum München, 85764 Neuherberg, Germany
[16]German Center for Diabetes Research, Helmholz Zentrum München, 85764 Neuherberg, Germany
[17]German Center for Neurodegenerative Diseases (DZNE), 81377 Munich, Germany
[18]Neuroproteomics, School of Medicine, Klinikum Rechts der Isar, Technical University of Munich, 81675 Munich, Germany
[19]Institute of Anatomy, University of Leipzig, 04109 Leipzig, Germany
[20]Institute of Computational Biology, Helmholz Zentrum München, 85764 Neuherberg, Germany
[21]TUM School of Life Sciences Weihenstephan, Technical University of Munich, 85354 Freising, Germany
[22]Department of Mathematics, Technical University of Munich, 85748 Garching, Germany
[23]NNF Center for Protein Research, Faculty of Health Sciences, University of Copenhagen, 2200 Copenhagen, Denmark
[24]These authors contributed equally
[25]Lead Contact
*Correspondence: mmann@biochem.mpg.de (M.M.), erturk@helmholtz-muenchen.de (A.E.)
https://doi.org/10.1016/j.cell.2022.11.021

SUMMARY

Spatial molecular profiling of complex tissues is essential to investigate cellular function in physiological and pathological states. However, methods for molecular analysis of large biological specimens imaged in 3D are lacking. Here, we present DISCO-MS, a technology that combines whole-organ/whole-organism clearing and imaging, deep-learning-based image analysis, robotic tissue extraction, and ultra-high-sensitivity mass spectrometry. DISCO-MS yielded proteome data indistinguishable from uncleared samples in both rodent and human tissues. We used DISCO-MS to investigate microglia activation along axonal tracts after brain injury and characterized early- and late-stage individual amyloid-beta plaques in a mouse model of Alzheimer's disease. DISCO-bot robotic sample extraction enabled us to study the regional heterogeneity of immune cells in intact mouse bodies and aortic plaques in a complete human heart. DISCO-MS enables unbiased proteome analysis of preclinical and clinical tissues after unbiased imaging of entire specimens in 3D, identifying diagnostic and therapeutic opportunities for complex diseases.

INTRODUCTION

At their early stages, many diseases have modest pathological changes in mostly unknown tissue regions, making them hard to identify and characterize. For example, early changes in dementia may include the activation of a few local inflammatory cells, changes in the microvasculature, and the appearance of just a few initial amyloid-beta plaques in uncharacterized brain regions.[1] Such small regional changes are extremely hard to identify using standard histology, limiting our ability to investigate initial stages of diseases for early diagnosis and therapy. Recent advances in tissue clearing technologies allow fluorescence imaging of complete biological tissues including mouse organs and whole bodies as well as intact human organs.[2–4] After tissues are rendered transparent, end-to-end laser scanning microscopy reveals their cellular and subcellular details. Leveraging artificial intelligence (AI)-guided image analysis, even tiny changes in cellular structures, which otherwise would be missed, can be identified readily and quickly.[5,6] However, visually pinpointing these regions alone does not answer mechanistic questions at the molecular level.

In parallel, enormous progress has been made to increase the throughput of single-cell transcriptomic technologies,[7–9] even though some studies show that RNA expression may weakly correlate with the protein expression.[10–13] More recently, single-cell analysis of proteomes has also become possible with the advent of ultra-high-sensitivity mass spectrometry (MS)-based approaches.[10,14–17]

At the RNA level, it is possible to preserve the spatial context in two-dimensional (2D) samples as spatially resolved transcriptome analysis is quickly becoming a mainstay of the molecular biology toolkit.[18–25] Methods for spatial proteome analysis are actively developed, but most methods are either limited to analyzing fewer than 100 proteins (e.g., highly multiplexed or multi-round immunostaining) or limited to 2D samples (e.g., MS-based spatial proteomics) or both.[26–30] In addition, it has been unclear to what extent these methods can be made compatible with advanced whole-organ imaging of optically cleared tissue.

Here, we combine whole-organ and whole-mouse tissue clearing and imaging with ultra-high-sensitivity MS-based proteome analysis and can characterize the proteome of samples isolated from cleared tissue comprising fewer than 100 cells. We term this method three-dimensional (3D) imaging of solvent-cleared organs profiled by mass spectrometry, or DISCO-MS (Figure S1A). Using DISCO-MS, we successfully analyzed fluorescently labeled small target regions isolated from whole mouse or human organs to discover spatial-molecular profiles of initial pathological events in various disease models (Video S1). To facilitate sample extraction, we developed a robotic tissue extraction system (called DISCO-bot) for more challenging specimens including whole adult mouse bodies and whole human organs (Video S2). Combining DISCO-MS and DISCO-bot, we studied the spatial proteome heterogeneity of immune cell-enriched tissues from bone marrow niches of intact mice and aortic plaques from the human heart.

RESULTS

MS-based proteomics of solvent-cleared tissue

Tissue clearing is a chemical process that relies on tissue permeabilization and subsequent extraction of different biomolecules including water (organic-solvent-based methods) and lipids (in most clearing methods).[31] Whether the proteome of tissues after these diverse extraction steps remains intact had been unclear. To investigate this, we employed MS-based proteomics, which can provide unbiased in-depth insights into the composition, structure, and function of the entirety of expressed proteins.[32]

To this end, we subjected solvent-cleared samples to proteomics workflows with respect to protein recovery and qualitative and quantitative reproducibility. Using fresh-frozen tissues as controls, we started with 3DISCO and uDISCO clearing methods (Figures S1B–S1D), two commonly used methods that are quick and known to provide the highest tissue and organ transparency.[3] We tested several protein-solubilization approaches and figured that the combination of SDS-based protein solubilization and tissue pulverization, followed by SDC resolubilization and protein digestion, yielded qualitatively and quantitatively very similar proteomes between fresh and solvent-based clearing methods (Figures S1B and S1C). We identified up to 5,500 proteins across conditions with Pearson correlation coefficients between 0.89 and 0.99 (Figure S1D).

While 3DISCO and uDISCO work well for fluorescent dye imaging, the signal of endogenous fluorescent proteins such as EGFP is rather unstable and decays with time.[33] To avoid this, we developed vDISCO, which uses fluorescent-dye-conjugated nanobodies to stabilize and enhance fluorescence signals.[34] As vDISCO includes several additional steps that might change proteome constitution, we also tested our proteomics workflow on these tissues. Identification of more than 6,000 proteins across all clearing conditions including vDISCO and replicates with Pearson correlations ranging from 0.85 to 0.94 confirmed the suitability of our workflow (Figure 1A). Next, we asked whether archived human brain tissues can be analyzed and cleared human brain tissue stored in formalin for more than 5 years with the DISCO and SHANEL methods.[4] DISCO-MS identified more than 5,000 proteins in all clearing conditions very similar to paraformaldehyde (PFA)-fixed controls at high quantitative reproducibility (R = 0.91–0.96) (Figure 1B). We conclude that our sample preparation workflow allows the MS-based proteome analysis of cleared mouse and human specimens at high depth and quantitative accuracy comparable to fresh and PFA-fixed control samples.

High proteome yield in vDISCO cleared tissues

Next, we examined the in-depth proteomes of vDISCO-cleared tissues to investigate potential protein depletions introduced by the clearing process and compared with fresh-frozen samples. We identified close to 8,000 proteins, a very substantial proportion of the total proteome across conditions and biological replicates with a high quantitative reproducibility (R = 0.94; Figure 1C and S2A). Coefficients of variation (CVs) within fresh (non-perfused) and cleared (perfused and fixed) conditions were below 0.2, demonstrating that vDISCO clearing yields proteomes that are qualitatively and quantitatively similar to fresh tissue and highly reproducible across biological replicates

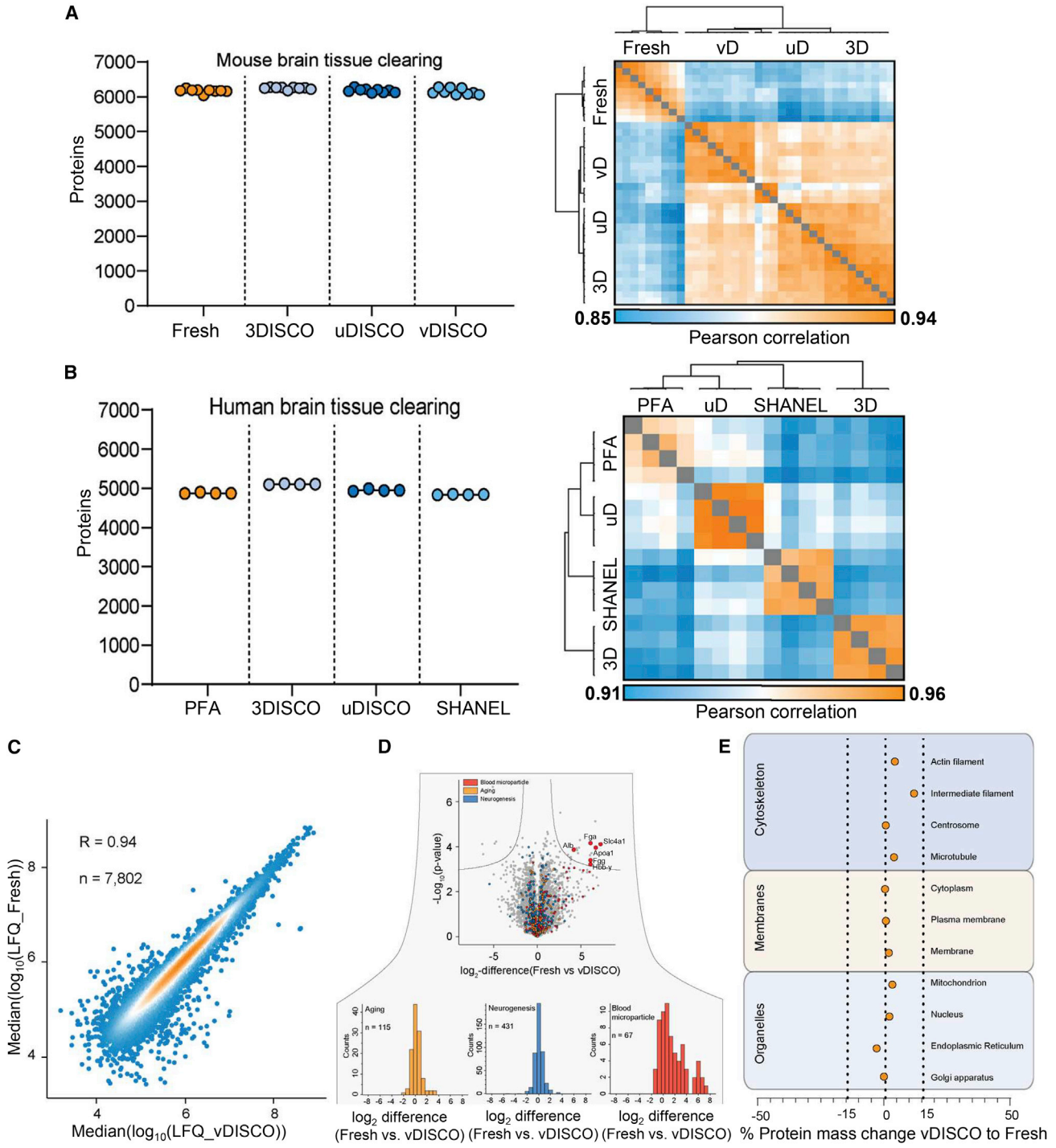

Figure 1. Proteome of cleared rodent and human tissues

(A) Proteome analysis from mouse brain tissues after different organic solvent-based tissue clearing methods vs. fresh controls. Protein identifications and proteome correlations across all clearing techniques and fresh tissue are shown. (N = 3 biological replicates, n = 9 total experimental replicates per condition).

(B) Archived human brain cortex blocks cleared and number of detected protein groups with proteome correlations across all clearing methods are compared with the numbers in PFA fixed blocks. n = 4 experimental replicates.

(C) Quantitative reproducibility of vDISCO-cleared vs. fresh.

(D) DE analysis of vDISCO-cleared vs. fresh sample proteomes highlighting the expected change in "blood microparticle" due to blood perfusion step for tissue clearing in contrast to fresh samples. Otherwise, proteins in other GO groups were unchanged.

(legend continued on next page)

(Figures S2B–S2E). The only altered gene ontology (GO) term was "blood microparticle" proteins, not surprising as fresh tissues were not perfused. Other GO keywords are quantitatively and qualitatively preserved (Figure 1D and S2F). Next, we checked the protein mass distributions between fresh and vDISCO mouse brains for membrane, organelle, and cytoskeleton terms. We found that all percentage protein mass differences were well below 15% across sub-terms and that the protein mass change associated with all membrane-related terms was below 3% (Figure 1E). Moreover, we also looked at the specific membrane-bound protein class, which are plasma membrane proteins. The percentage total protein mass change was below 0.5%. As an example, we highlighted epidermal growth factor receptor (EGFR), a transmembrane receptor, between fresh and vDISCO-cleared brain samples (Figure S2G). In summary, even the strongest organic solvent-based tissue clearing approach, vDISCO, yields qualitatively and quantitatively very similar proteomes compared to the fresh tissue.

Proteomes of micro-dissected tissues imaged in 3D

After establishing a high-quality and reproducible MS-compatible sample preparation workflow for solvent-cleared tissues, we turned to the unbiased proteome analysis of smaller target tissue regions (~0.0005 mm^3) previously imaged and located in 3D. We successfully met three major challenges: (1) reliable dissection of small tissue regions identified by 3D imaging of cleared tissues, (2) analysis of deep proteomes from only a few nanograms of dissected and rigid solvent-cleared tissue, and (3) registration of small tissue regions back onto a complete 3D light-sheet image stack. To solve the first challenge, we developed a series of steps to render cleared rigid tissue soft for precise cryo-sectioning and laser capture microdissection (LCM) without deformation. In short, we reversed the clearing protocol, rehydrated the cleared tissue stepwise, and cryo-preserved it. This workflow avoided rupturing of the tissue during cryo-sectioning and allowed us to laser micro-dissect tissue regions as small as 0.0005 mm^3 corresponding by volume to approximately 60 cells. Next, we miniaturized our sample preparation workflow and then performed MS-based proteome analysis on a modified trapped ion mobility MS platform developed for highest sensitivity down to the level of single cells.[10] Lastly, we automated registration of the 2D LCM images back to the 3D light-sheet imaging stack (Figure 2A). Briefly, following light-sheet microscopy imaging, the cleared mouse brains were rehydrated, cryoprotected, sectioned, and imaged prior to cutting by LCM. These images were aligned (rigid registration) to produce a reconstructed 3D stack of LCM sections. These were then coordinated slice by slice to a subset of the light-sheet imaging stack (affine registration), and the highest-scoring section was subsequently used to project the regions of interest (ROIs) onto the 3D light-sheet imaging data (Figure 2B and S3Q; see Methods S1).

To explore the potential of our technology in biological applications, we first used a mild traumatic brain injury (mTBI) mouse model to identify and analyze proteomes of brain regions containing discrete local inflammation. mTBI and concussions are common injuries that can lead to long-term morbidities such as sleep disorders, neuropsychiatric disorders, and even early onset of dementia.[35] They are characterized by chronic inflammation, which can induce neurodegeneration in selected brain regions, particularly along the stretched axonal tract.[36] We used a repetitive mTBI injury model on CX3CR1-EGFP mice (Figures S3A and S3B), in which all microglia are labeled with an EGFP-fusion construct. The mild nature of this injury was confirmed by behavioral test that showed no significant alterations after 8 weeks post injury in Barnes maze and beam-walk tests (Figures S3C and S3D). Brains of CX3CR1-EGFP mice were processed for vDISCO labeling and clearing 8 weeks post injury, showing microglia activation in discrete regions of whole brain. ClearMap quantification[37] identified activated microglia with enlarged morphology in diverse brain regions, especially along the axonal tracts including the optic tract and the corpus callosum when compared with sham-operated animals (Figures S3E–S3L). The same mTBI injury model on Thy1-GFP-M reporter mice (expressing GFP only in neurons) confirmed the axonal abnormalities in the same brain regions (Figures S3M–S3P).

We then used DISCO-MS on isolated ROIs including locally activated microglia with known spatial information (Figures 2B and 2C; Video S3). Analyzing three ROIs from the optic tract as small as 0.0005 mm^3 compared to corresponding regions in sham control animals, we quantified up to 1,400 proteins per ROI. Overall, we found 602 common proteins in all ROIs of mTBI and sham. Comparing ROIs from mTBI among themselves, we found a shared proteome signature comprising 717 proteins, with each ROI having unique sets of proteins (Figure 2D). Principal-component analysis (PCA) separated the proteomes of ROIs between mTBI and controls (Figure 2E). Interestingly, several proteins related to axonal damage and repair were strongly differentially regulated between conditions. For example, stathmin1 (Stmn1; 32-fold increase) is a protein involved in the regulation of microtubule filament system. Its overexpression has been shown to promote disassembly of microtubules in blast-induced mTBI.[38] Neurocan (Ncan; 30-fold increase) is a chondroitin sulfate proteoglycan involved in the modulation of cell adhesion and migration, which is upregulated in injured brains.[39] Eight proteins were uniquely detected in mTBI, including metadherin (Mtdh) present in glial cells but not yet been described in mTBI. Furthermore, we found many previously described proteins in the context of brain injury, providing positive controls, and many yet unknown proteins to be downregulated in the mTBI model. For example, acid ceramidase (aCDase, Asah1), an enzyme implicated in sphingolipid metabolism and in multiple diseases, was downregulated[40–42] and has previously been associated with morphological defects in cultured neurons.[43] Our data now suggest its potential involvement in axonal deformity in mTBI. We also observed alterations in mitochondria proteins along the optical tract such as caseinolytic protease proteolytic subunit (Clpp), a mitochondrial matrix

(E) Percentage change of protein mass distribution between vDISCO-cleared vs. fresh samples. Percentage changes are shown as a median change within one group for organelles, membranes, and cytoskeleton GO terms (N = 3 biological replicates, n = 9 total experimental replicates per condition).
See also Figures S1 and S2.

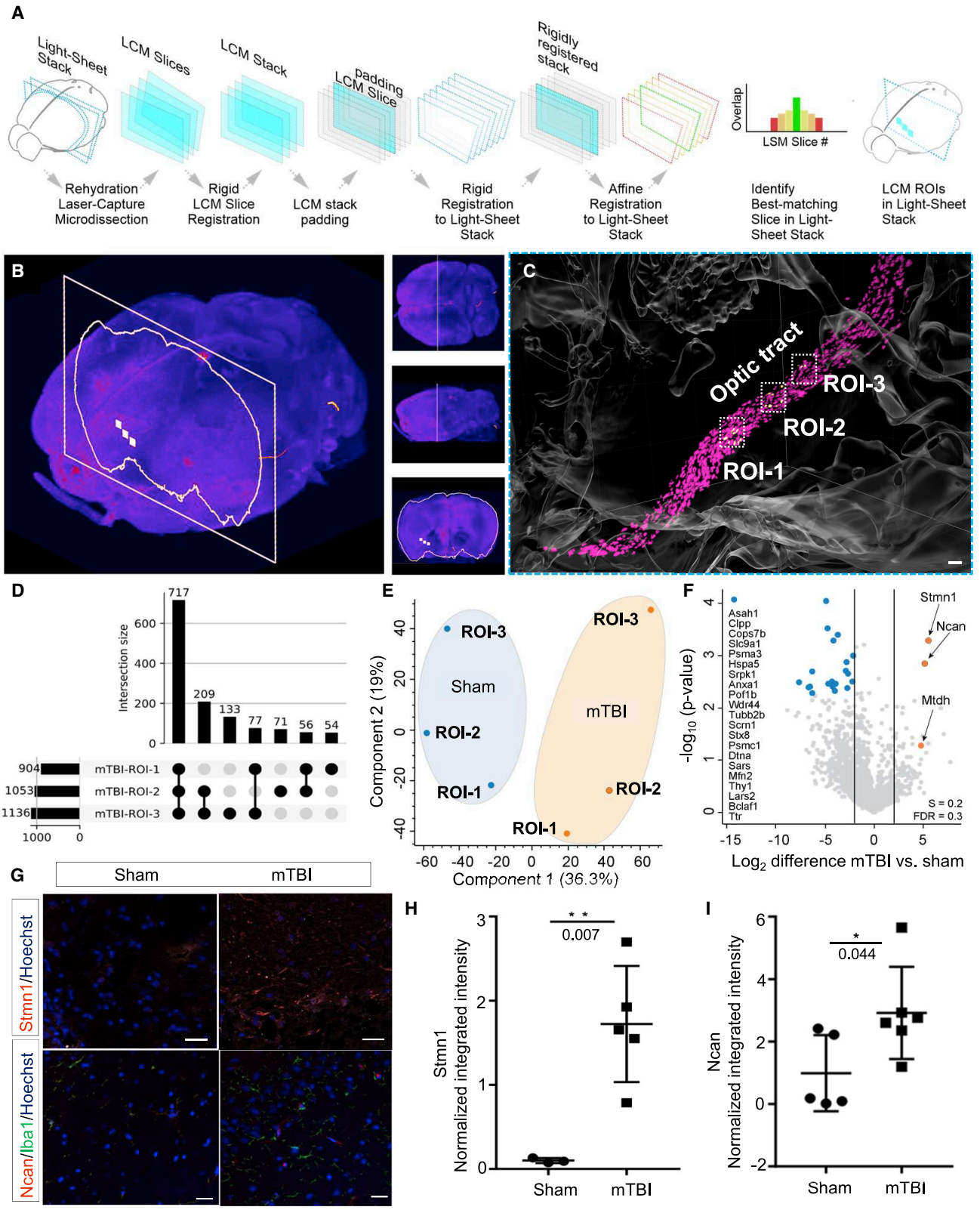

(legend on next page)

protease,[44] and mitofusin 2 (Mfn2), a mitochondrial membrane protein that participates in mitochondrial fusion and contributes to the maintenance and operation of mitochondrial network[45] (Figure 2F). We further validated the enrichment of Stmn1 and Ncan in mTBI brain tissues by immunofluorescence (Figures 2G–2I). Our data demonstrate that DISCO-MS is a powerful approach for obtaining unbiased proteomic information on heterogeneous tissue regions with known spatial locations.

Scalable and robust pathology identification using deep learning

One of the early hallmarks of Alzheimer's disease (AD) pathology is the accumulation of amyloid-beta (Aβ) plaques in the brain parenchyma.[46] We anticipated that the unbiased detection of Aβ plaques, followed by their equally unbiased proteome analysis using DISCO-MS, would provide valuable insights into the initial stages of AD. To this end, we used the 5xFAD mouse model of AD to identify Congo red labeled Aβ plaques in young mouse brains.

As the locations of these initial plaques are unknown, we developed a deep learning (DL) approach to identify all Aβ plaques rapidly and reliably in whole mouse brain scans. In short, our network architecture is based on U-Net, a well-established approach for biomedical image analysis[47] (Figure 3A). To assess our segmentation quality, we calculated a wide range of voxel-wise and Aβ plaque segmentation metrics. Our DL architecture for automated Aβ plaque detection showed high performance in volumetric accuracy (0.99 ± 0.00), volumetric (0.71 ± 0.06), and surface (0.94 ± 0.03) as well as overall Dice scores (0.89 ± 0.09) per Aβ plaque. After segmenting all plaques in the entire brain using DL, we registered our data to the Allen brain atlas to obtain region-wise quantifications for over a thousand brain subregions (Figure 3B).[48,49] We then grouped them into the major brain regions as defined by the Allen mouse brain ontology for simplicity and visualized plaque volume per region in early and later stages of disease (Figures 3C and 3D) using brainrender-an open source Python package for interactive visualization.[50]

Our DL model identified few Aβ plaques in 6-week-old mouse brains and identified several thousand at a later stage of the disease (6-month-old 5xFAD), (Video S4) whereas plaques were absent at 5 weeks of age. We also confirmed our finding of Aβ plaques in 6-week-old mice in the same brain regions by immunohistochemistry with anti-Aβ monoclonal antibodies (Figure S4A). To compare the plaques between 6-week- and 6-month-old 5xFAD mice in 1,238 different brain regions, we grouped 72 major brain regions according to Allen brain atlas and plotted 27 disease-relevant regions. Some of the main brain regions with initial plaques were retrohippocampal region, medulla, molecular layer of cerebellar cortex, fiber tracts, subiculum areas, visual area, and hippocampal formation. The subiculum area and retrohippocampal region showed much larger number of plaques at later stage (6 months) of disease: 1,689 and 10,630, respectively (Figures 3E and 3F). We observed the largest plaques in the midbrain (motor related, 3,438 μm^3) followed by temporal association areas (2,880 μm^3), posterior amygdalar nucleus (2,450 μm^3), and auditory areas (2,366 μm^3), with an average volume ranging between 2,000 μm^3 and 3,500 μm^3 in early stage (Figure 3G). Interestingly, the plaque volume of these regions were significantly reduced at 6 months, indicating a temporal change in plaque morphology, either caused by adverse biological effects by their surrounding microenvironments or potentially causing changes to it during disease progression.

Following the DL-based identification of early Aβ plaques in the 5xFAD mouse model, we isolated four ROIs (volume: ~0.0005 mm^3) from the hippocampal region vs. corresponding brain regions from the control mice and subjected them to MS-based proteomics (Figures 4A–4D). We compared ~2,000 proteins across replicates and PCA plot separated the ROIs with Aβ plaques from the control brain regions (Figure 4E). Differential expression (DE) analysis revealed that many well-characterized AD-associated proteins were enriched in 5xFAD ROIs including the Aβ precursor protein,[46,51] (32-fold increase) and the thimet oligopeptidase 1 (8-fold increase) (Figure 4F). Apart from known and well-established AD-related proteins,[52,53] we also detected less-characterized proteins in early-stage Aβ plaques such as a member of the calcium-binding protein family S100a11.

Moreover, we asked how similar the proteomes of our ROIs with early Aβ plaques were compared to each other. Plaques with more than 1,200 protein identifications each shared 768 proteins, defining a core proteome of early-stage Aβ plaque formation (Figure 4G). An abundance rank plot of the shared early-stage Aβ plaques' core proteome revealed several members of the Ywhaz (14-3-3) and the S100a protein family. In the early-stage Aβ plaque ROIs, we also found many other proteins involved in AD such as two isoforms of Mapt, namely Mapt-4 and Mapt-5, illustrating the specificity of MS-based proteomics (Figure S5A). Our proteomics data also highlight early-stage Aβ plaque variability (Figure S5B) with respect to well-characterized AD proteins (Mapt, Tmed10, App), proteins of the S100a family,

Figure 2. DISCO-MS reveals effects of mTBI in discrete regions of whole brain

(A) Schematic representation of the alignment procedure.

(B) Location of the LCM slice (outline) inside the light-sheet stack, with the dissected 200 × 200 μm areas (white squares) inside the optic tract.

(C) 3D reconstruction of stiched images of an exemplary CX3CR1-GFP/+ mouse brain after mTBI, highlighting substantial increase in activated microglia (in magenta) along optic tract region. 3 neighboring ROIs along optic tract were identified, laser captured, and subjected to proteomic analyses. Scale bar, 100 μm.

(D) The number of shared and unique set of proteins in mTBI.

(E) PCA plot showing the distribution of individual ROIs from mTBI vs. ROIs from control (sham) with the same spatial location.

(F) Volcano plot showing the significant enrichment of proteins.

(G) Histological validation of the top 2 proteins in the optic tract: (1) stathmin (Stmn1) in red and nuclear marker Hoechst dye in blue, (2) neurocan (Ncan) shown in magenta along with microglia marker (Iba1) in green and Hoechst dye in blue. Scale bars, 20 μm.

(H and I) Intensity quantification of Stmn1 immunostaining signal ($p = 0.007$, $n = 3$ from total 8 sections) and Ncan immunostaining signal ($p = 0.044$, $n = 3$, animals from total 11 sections) in mTBI vs. sham, respectively (unpaired two-sided Student's *t* test, data presented as ± SD).

See also Figure S3, Methods S1, and Video S3

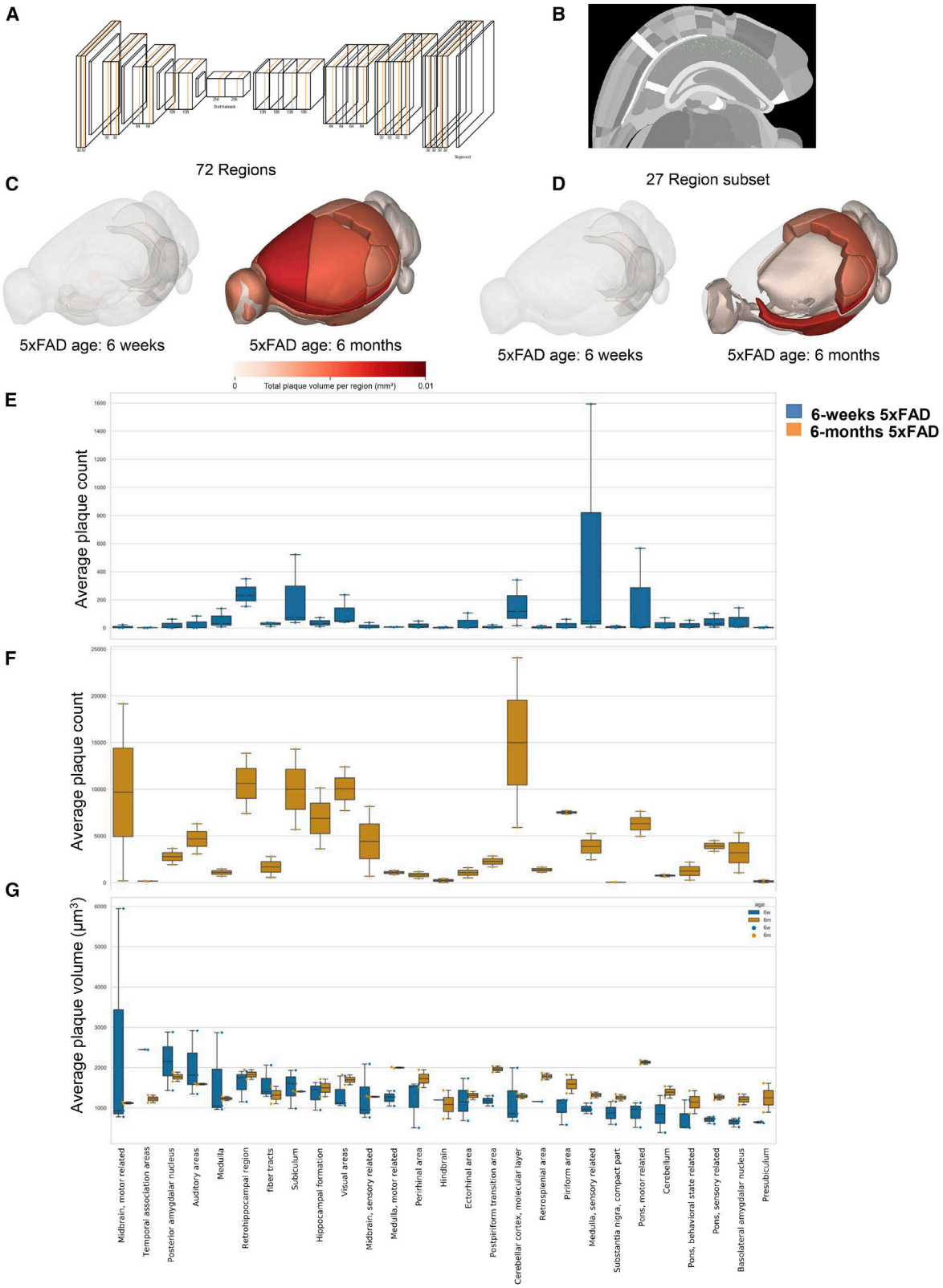

(legend on next page)

peptidases (Thop1, Ppia), proteins of the Ywha family, and other structure-determining proteins including Nefm and Map2. Finally, we confirmed the presence of S100a11 and Thop1 in early-stage plaques of 5xFAD brain slices by immunofluorescence, whereas these proteins are absent from the respective regions in wild-type (WT) mice (Figures S4B–S4D).

We next compared plaque regions to neighboring non-plaque regions in the dorsal and ventral subiculum, where we observed initial plaque formations (Figures 4H and 4I). We found that 29 proteins were upregulated whereas 14 proteins were downregulated in these early plaque isolates. Among others, we found significant quantitative change of proteins related to vesicle fusion, vesicle-mediated transport, and secretory pathways (Bnip1, Cpd; >10-fold increase in both; $p < 0.0001$ for Bnip; $p < 0.05$ for Cpd), which are potential markers for an early AD onset (Figure 4K). Known plaque-associated proteins were regulated in a region-specific manner, which were previously identified only at the later stages of AD without precise spatial location (Figure 4L). For example, an increased expression of Manf had been reported in APP/PS1 transgenic mice only at later stages of the disease.[54] Actl6b is involved in transcriptional activation and repression of select genes by chromatin remodeling and has been investigated in in the context of later-stage AD (6–15 months).[55] Mutations in human Actl6b have been associated with intellectual disability,[56] suggesting a role of this protein in the early stage of neurological conditions, including AD. Mbp, Cnp, and Plp1 have been associated with the structural integrity of the myelin sheath and its function in age-related AD.[57] In addition to many significantly enriched proteins in early plaques vs. non-plaque areas of the same region, we also found substantial subregional heterogeneity (Figures S5C–S5E). Furthermore, many of these proteins were uniquely distributed across these two subregions. These could potentially drive disease progression in a region-specific manner, a concept that has been little explored thus far due to technical limitations.

Next, we profiled the later-stage plaque (6 months) microenvironment in a region-specific manner and compared this with early plaque protein enrichments (Figures S5F and S5G). Dorsal subiculum data showed a significant upregulation of 49 proteins, whereas 21 proteins were downregulated. Among the upregulated proteins, we found proteins related to S100a family (S100a13), complement activation and microglia phagocytosis pathway (C1qa, C1qb, Itgb), and tau protein binding (Apoe, S100b, Clu). We also observed a distinct proteomic signature in dorsal vs. ventral subiculum at later stages, indicating region- and time-specific changes in the proteomic landscape around these plaques (Figures S5H and S5I).

Taken together, DISCO-MS allowed us to pinpoint early- and late-stage Aβ plaques from the whole brains in 3D and analyze their spatial proteomic makeup. We recovered many known markers of Aβ plaques in AD as well as less-characterized proteins in AD pathogenesis. Our data also suggest the significant involvement of S100a, Ywhaz (14-3-3), vesicle fusion and transport, myelin sheath function, and the complement system related family members in early-stage Aβ plaque development.

DISCO-MS from large-volume samples by DISCO-bot tissue extraction

Next, we aimed to develop DISCO-MS for even larger samples including whole mouse bodies and whole human organs. As sectioning/imaging for LCM is impractical for large-volume samples at scale, we developed a robotic extraction system (named DISCO-bot), using biopsy needles to isolate ROIs for subsequent proteomics analysis (Figure 5A). This required (1) stabilization of whole mouse body for robotic extraction while imaging, (2) minimizing biopsy needle deflections during extractions, and (3) biopsy needles that can penetrate into hard cleared tissues.

Firstly, to stabilize the sample, we investigated different resins and agarose concentrations to modulate bed stiffness, compatibility with the clearing solutions, and imaging and figured that 2% agarose embedding was well suited for our purpose. Next, we customized different 3D-printed mouse holder adaptors and needle holders, according to their strength and force-deflection criteria and chose the one with the least deflection (Figure 5B–5E and S6). Last, we tested various needle sizes and shapes with stylet inside and found that needles size 18 gauge (G) and/or 22 G provided a good penetration and sample extraction precision without contamination of undesired tissue (Figure 5F; see details in STAR Methods). We further optimized the DISCO-bot to work concomitantly with the light-sheet microscope (Figures 5G–5I). The resulting DISCO-bot system allowed the extraction of small tissue regions from cleared samples while imaging, thereby enabling non-destructive and repetitive tissue isolation at scale for DISCO-MS (Figures 5J–5M; Video S5; see DISCO-MS Handbook as Methods S1).

To demonstrate the utility of the DISCO-bot in our DISCO-MS pipeline, we cleared LysM-eGFP mice using vDISCO. We co-labeled nuclei with propidium iodide (PI) to identify the ROIs for DISCO-bot extraction. Imaging of the whole body allowed us to spatially identify locations of all LysM-eGFP$^+$ cells, which were mostly found to be in bone marrow niches (Figure 6A; Video S6). We then focused on the cranium and scapula, two bones with irregular 3D structures and thus hard to study with standard 2D sections. We chose three ROIs from the parietal cranium region and six ROIs from scapula (three from the lateral border (LysM-eGFP) and three ROIs from the medial border (LysM-eGFP$^+$) [Figures 6B–6E]). DISCO-bot-extracted ROIs were then

Figure 3. Deep learning analysis of plaques in whole 5xFAD mouse brains

(A) 3D U-Net architecture including layer information and feature sizes.

(B) Segmented plaques overlaid on the hierarchically and randomly color-coded atlas to reveal annotated regions available.

(C) Visualization of plaque volume per region in 72 regions.

(D) Visualization of plaque volume per region in a subset of 27 major regions.

(E) Quantification of the number of plaques in the major brain areas of 6-week-old mice (n = 3, ±SD).

(F) The number of plaques in the major brain areas of 6-month-old mice (n = 2, ±SD).

(G) Quantification of the plaque volume in 6-week-old mice (in blue, n = 3, ±SD) and 6-month-old mice (in orange, n = 2, ±SD).

See also Video S4

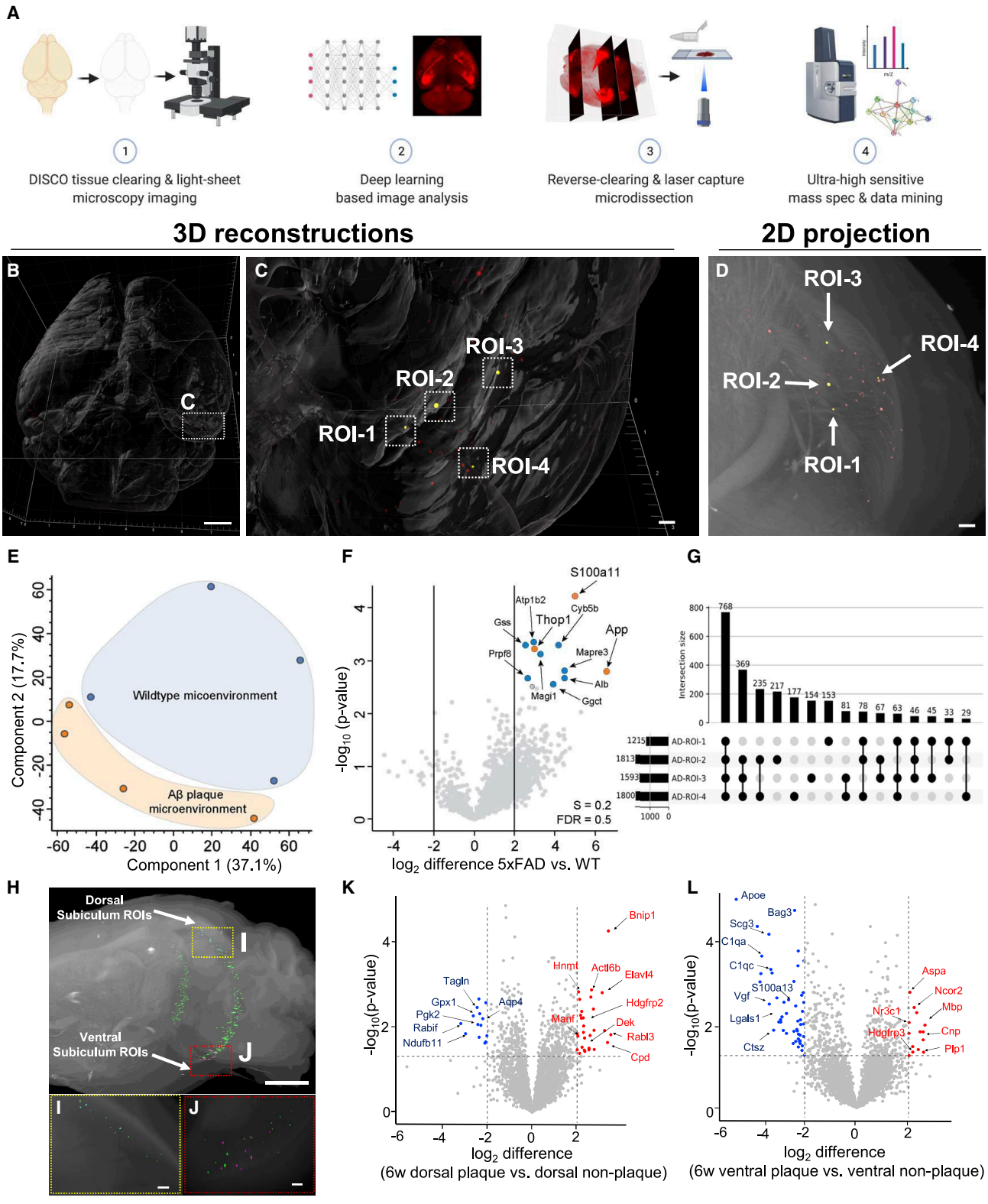

Figure 4. DISCO-MS unravels the single-plaque proteome in AD mouse model

(A) Major steps of DISCO-MS.

(B) 3D visualization of Aβ plaques (in red) in stiched images of 5xFAD mouse brains (n = 4 experimental replicates). Scale bar, 500 μm.

(legend continued on next page)

analyzed using the DISCO-MS pipeline as described above. In the cranium, we identified the shared signature of 1,984 proteins in all three ROIs with Pearson correlation between 0.72 and 0.76 (Figures 6F and 6G). To verify the precision of DISCO-bot extraction, we compared our results with proteomics of freshly isolated skull marrow cells.[58] We found ~2,200 shared proteins out of total 2,550 identified protein groups when compared with isolated skull-proteome, confirming the high precision of DISCO-bot extraction. Among others, seven protein groups identified here were earlier shown to be expressed both at transcript and proteome level in freshly isolated skull marrow, which further validates the extraction precision using robotic arm (Figure 6H). In the scapula, we observed distinct signal of LysM-eGFP in medial vs. lateral border bone. PCA clearly separated the two groups as well as the ROIs itself, particularly from medial border, indicating inter-regional and intra-regional heterogeneity among these extracts. We identified 1,250 proteins across conditions with high Pearson correlation coefficients (0.88–0.98) and found a common signature of 764 proteins between lateral and medial border bone, whereas 336 and 22 proteins were unique to the respective regions (Figures S7A–S7C). DE analyses showed upregulation of ten proteins, including those related to the innate and adaptive immune system such as antigen-presenting molecule H2-L (MHC class1b), B cell/T cell receptor pathway-related proteins, and cytokine signaling proteins such as signal transducer and activator of transcription 3 (Stat3), which are involved in biological processes of inflammatory response regulation to antigenic stimuli. Among 33 downregulated proteins were signalosome-related proteins (Cops7a) and proteins related to actin filament network formation (Fhod1) (Figure 6I–6L and S7D). These results demonstrate that DISCO-MS can be applied to whole adult mouse bodies after end-to-end imaging to investigate spatial-molecular heterogeneity and diverse biology.

Spatial proteomics of coronary arteries in SHANEL-cleared human heart

Next, we tested our DISCO-bot-aided DISCO-MS approach in coronary artery disease (CAD). Acute myocardial infarction (MI) is the major contributor to cardiovascular mortality, the leading cause of deaths worldwide.[59,60] It occurs when atherosclerotic plaques (largely made up of lipids and calcified tissue) slowly build up in the inner lining of a coronary artery and then suddenly rupture, causing thrombus formation, occluding the artery and ultimately prevent blood flow to other parts of body. Recent advances in single-cell RNA sequencing (scRNA-seq) technologies have provided a deeper understanding of cardiac cells in both health and disease[61,62] but lack precise spatial information. Moreover, transcript levels may weakly correlate with proteome data, even at the single cells.[10]

We obtained PFA-fixed human heart, labeled its vessels with dextran, and cleared the whole heart using SHANEL human organ clearing protocol (Figures 7A and 7B). This readily located the calcified atherosclerotic plaques of any size along regions without plaques in the same coronary artery. We extracted six ROIs around the large plaque-associated regions and six ROIs from the little-to-no plaque-associated regions, which could represent early plaque formation along the coronary artery of the same heart for DISCO-MS analysis (Figures 7C–7F; Video S7). We quantified 1,300 proteins in each ROI and found 53 downregulated and 6 upregulated proteins (Figure 7G). Systematic GO term and pathway analysis of regulated proteins suggests the regulation of hypertrophic cardiomyopathy, cardiac muscle contraction (TPM1, TPM2, MYL2, MYL3, MYH6, MYBPC3, DES), focal adhesion, blood coagulation, plasminogen activation, platelet aggregation, fibrinogen complex, blood-clotting cascade (SERPING1, FGA, FGG, FGB, FN1) (Figure 7H, S7E, and S7F). Some of these proteins were regulated in a region-specific manner including MYH10, MYH11, FGA, FGB, and FGG, which have already been reported to be associated with plaques (Figure 7I). Furthermore, we found upregulation (2.2-fold, $p < 0.05$) of myosin heavy chain (MYH8), a less-characterized protein in context of atherosclerotic plaque. As its related forms MYH10 and MYH11 were recently discovered as biomarker for atherosclerotic plaque formation,[63,64] our findings of MYH8 in the context of CAD is encouraging and invites further investigation. We also observed a 2.5-fold ($p < 0.01$) increase in glyoxalase 1 (GLO1), a ubiquitous cellular enzyme that participates in the detoxification of methylglyoxal, a cytotoxic byproduct of glycolysis that induces protein modification (advanced glycation end products, AGEs), oxidative stress, and apoptosis. GLO1 and AGEs are implicated in the pathogenesis of aging and diabetes. A large-scale meta-analyses showed a gene network involved in antigen processing to be strongly associated with CAD.[65] Key drivers of this network included GLO1, which strengthens the potential role of this protein in reprogramming atherosclerotic plaque microenvironment. We also observed a significant enrichment (2.3-fold, $p < 0.01$) of carbonic anhydrase 6 (CA6), which might play a role in vascular calcification, hence plaque progression, and has not been associated with CAD before. CA are a group of isoenzymes that catalyze the reversible conversion of carbon dioxide into bicarbonate. CA isoenzymes were previously shown to be involved in the vascular calcification in humans.[66,67] We further found perturbations in members of recently discovered myosin heavy-chain family

(C) Enlarged view of region marked in (B) 4 different ROIs (in yellow) from hippocampus, each containing single-plaque, selected and isolated for mass spectrometric measurements. Scale bar, 100 μm.
(D) 2D projection of selected ROIs. Scale bar, 100 μm.
(E) PCA plot of ROIs' proteome from 5xFAD vs. the same regions from control.
(F) Volcano plot showing the significantly enriched proteins.
(G) The number of shared and unique sets of proteins in 5xFAD.
(H) Selection of early plaque and non-plaque ROIs from 2 subregions of subiculum. Scale bar, 1,000 μm.
(I and J) Enlarged view of regions marked in (H). Scale bar, 100 μm.
(K) Volcano plot showing significantly enriched proteins in plaque vs non-plaque areas in dorsal region.
(L) In ventral region (n = 14–20 ROIs per region).
See also Figures S4 and S5 and Video S1.

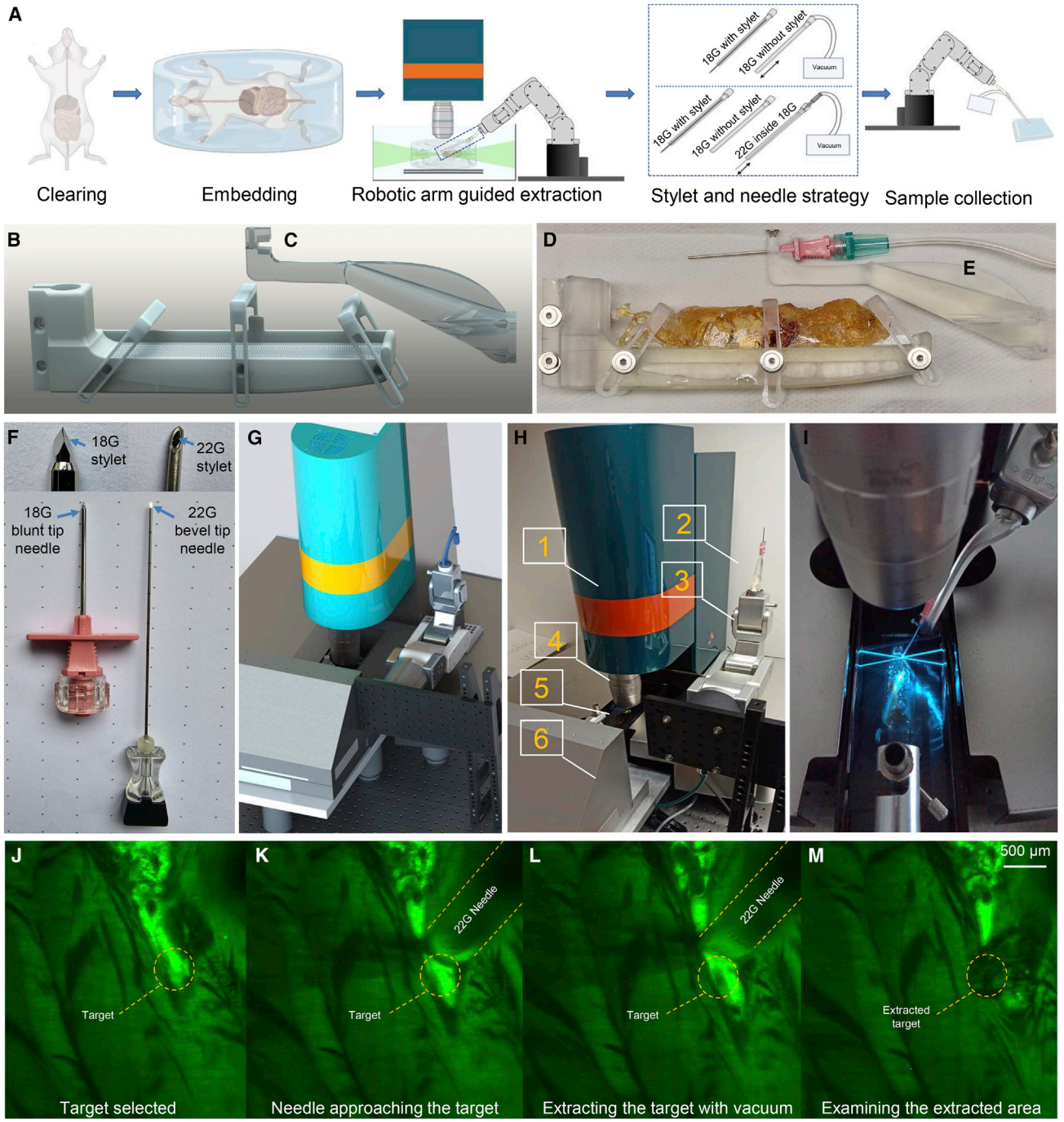

Figure 5. DISCO-bot enables non-destructive tissue extraction from large, cleared samples while imaging

(A) Schematic of robotic extraction.
(B) 3D model of the mouse holder.
(C) 3D model of needle holder.
(D) Cleared mouse on optimized mouse holder.
(E) Needle attached to the needle holder.
(F) The biopsy needles with sealing stylets.
(G) CAD model of microscope with robotic arm.
(H) Components of microscope and robotic setup annotated as (1) light-sheet microscope, (2) needle attached on the needle holder, (3) Meca500 6 DoF robotic arm with vacuum tube, (4) objective, (5) sample mounted on the mouse holder, (6) mouse holder stage.
(I) Meca500 robotic arm.

(legend continued on next page)

(MYH10, MYH11) biomarker and MYH6, a less-characterized form in the context of late-stage atherosclerotic plaque microenvironment. Moreover, we observed a significant reduction in the expression of MACROH2A.1 histone, which has been little studied in context of regulating autophagy and cholesterol efflux.[68]

DISCUSSION

Deciphering tissue heterogeneity is essential to understand normal physiology and pathological processes. However, despite the enormous progress made in single-cell and spatially resolved -omics technologies,[7–10,14–17] spatial-omics analysis of tissue regions imaged in whole organs and organisms remained challenging.

We addressed this challenge by developing and applying DISCO-MS for proteome analysis of small tissue regions identified by panoptic imaging of large samples, *in silico* 3D reconstructions using AI, and automated minimally invasive tissue isolation for large-volume tissues using robotics. Employing DISCO-MS, we identified brain regions affected by the early stages of Aβ plaque genesis in the brains of a young AD mouse model. Most of the initial plaques appeared in the retrohippocampal regions, including the entorhinal area, and some in hindbrain regions, including pons and medulla.[69] The proteome data provided by our work can facilitate the discovery of diagnostic and therapeutic approaches tailored for an early-stage intervention of AD. Future studies are warranted as, e.g., time course and molecular details might differ between the 5xFAD mouse model we used and other widely employed models such as the 3xTg-AD mice.[70] Our method also allows the analysis of human postmortem samples to explore the clinical relevance of our findings.

Earlier studies obtained the proteomic profiles either from the lysed whole brains of AD mice[71] or provided only average information on the plaque pathology from pre-selected brain regions without spatial details on the whereabouts of the plaques.[72,73] Moreover, some of these studies were performed only on certain isolated cell types or brain sections,[74,75] again missing the spatial context at the whole-organ level. More recently, attempts were made to characterize the plaques in whole brains of 5xFAD mice; however, these studies lack spatial proteome information.[76,77] In contrast, we obtain the proteomic data on isolated single-plaque microenvironments with the known spatial locations in whole brains. Thus, we provide both molecular information related to single plaques, and their spatial location, which would be critical for localized targeted treatments.

Our technology performs equally well on mouse and human tissues and yields qualitative and quantitative proteomics data nearly indistinguishable from uncleared samples, even for the harshest organic solvent-based tissue clearing approaches. The broad compatibility with different tissues and organisms and the relative ease of the DISCO-MS procedure will allow benchmarking different animal models against human samples on the molecular and anatomical levels.

Although tissue clearing presumably removes the lipidic cast of membrane proteins, we observed that the plasma membrane protein GO class was hardly affected, suggesting that DISCO-MS can be used to identify surface markers for drug targeting. Beyond neuroscience, this technology may transform spatial molecular investigations in many other biomedical research areas including clinical samples. We already applied DISCO-MS to human heart samples with atherosclerotic plaques and identified molecules involved in CAD such as GLO1, CA6, MYH6, and MACROH2A.1. After SHANEL clearing, we quickly navigated through the whole coronary artery in 3D and pinpointed the spatial distribution of plaque-associated regions. Given the precision and sensitivity of our method, we were able to isolate and analyze neighboring tissue regions with and without pathology for comparison.

A key advantage of our approach is that the robot-guided extraction of tissue isolates directly from the cleared tissue makes it scalable, as no prior sectioning and registration is needed. This allows the quick streamlined isolation of many samples from identical specimens while retaining complete spatial information and allowing for the resampling of other parts of the same specimen in future analyses.

In conclusion, we present a spatial unbiased proteome profiling technology comprising complete 3D-imaging data of whole organs and organisms, enabling unbiased identification and automated extraction of interesting tissue regions and including subsequent molecular characterization. Notably, the DISCO-MS technology presented here is versatile across labeling and solvent-cleared methods for whole organs. It is not only applicable to reporter mouse lines but can also be utilized where reporter lines are unavailable. In those cases, deep tissue labeling with dyes and potentially antibodies can be performed against the antigen of interest, imaged as a whole organ, and subjected to MS-based proteome profiling. DISCO-MS should be of great interest to researchers with archived solvent-cleared organs and imaging data, where molecular data are missing. This method will further enable to interrogate the molecular basis of a pathological milieu located in a seemingly random manner to advance research in complex diseases.

Limitations of our study

Although we have demonstrated that DISCO-MS enabled us to perform unbiased proteome analysis after unbiased imaging of entire specimens in 3D, further developments would be needed to extract fewer cells for downstream proteome analyses. Our current method works well for down to about 60 cells and provides us with average molecular details of these cells and their microenvironments. While this is sufficient to study diverse biological questions such as plaque heterogeneity, it is still far from the single-cell level. Single-cell resolution is important to understand the cell compositions and cellular interactions in the biological processes under investigation. To reach that goal, the current protocol needs to be refined for smaller sample

(H and I) Coarse calibration with mouse in imaging chamber prior to extraction.
(J–M) Robotic extraction example: (J) target selection, (K) needle approaching the target, (L) extracting the target under vacuum, (M) evaluation of extracted region.
See also Figure S6, Methods S1, and Videos S2 and S5

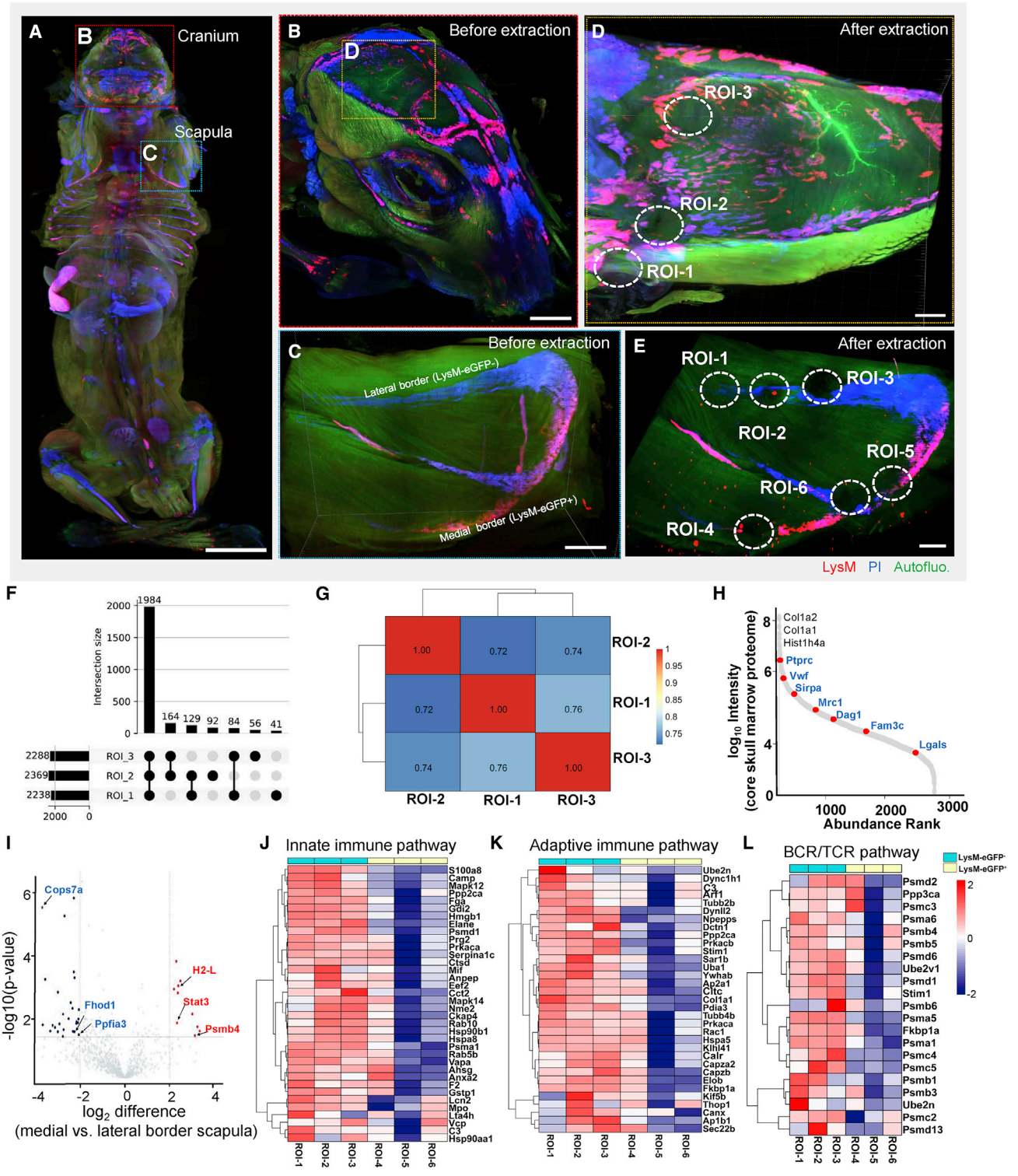

Figure 6. DISCO-bot-aided DISCO-MS on bone marrow niches of whole mouse bodies

(A) Stiched images of whole body of LysM-EGFP mouse after clearing and imaging (n = 4). Scale bar, 700 μm.

(B) 3D visualization of stiched images of whole head zooming into parietal surface before extraction.

(C) 3D visualization of stiched images of right scapula showing lateral and medial borders before extraction (PI in blue, LysM in red). Scale bar, 500 μm.

(D) Marked 3 ROIs in parietal surface after robotic extraction. Scale bar, 500 μm.

(E) Marked 6 ROIs, 3 in lateral border and 3 in medial border after extraction. Scale bar, 500 μm.

(legend continued on next page)

volumes to extract sub-nanogram tissues from the cleared samples. Furthermore, the proteomic sample preparation for cleared tissues could be miniaturized to the level of single cells or pooled cell states without losing proteomics depth.[17]

STAR★METHODS

Detailed methods are provided in the online version of this paper and include the following:

- KEY RESOURCES TABLE
- RESOURCE AVAILABILITY
  - Lead contact
  - Materials availability
  - Data and code availability
- EXPERIMENTAL MODEL AND SUBJECT DETAILS
  - Animals
  - Human samples
- METHOD DETAILS
  - Repeated closed head mild traumatic brain injury (mTBI)
  - Perfusion and tissue preparation
  - Congo red labeling of whole brains of 5xFAD animals
  - Clearing of brains using DISCO methods
  - vDISCO whole-brain passive immunostaining, clearing and imaging
  - vDISCO whole body immuno labeling, clearing and imaging
  - SHANEL sample preparation and clearing
  - Behavioral assessment
  - Immunofluorescence and confocal microscopy
  - Light-sheet microscopy and image processing
  - Registration of light-sheet and LCM images to correlate probe selection
  - Optimization of cleared tissue for cryopreservation and sectioning
  - Laser-capture microdissection
  - Automated robotic proteomic probe extraction from whole body
  - Precision and accuracy of sampling
  - Needle gauge
  - Specimen holder and needle holder strategy
  - Embedding of the whole mouse body
  - Manipulation system
  - Optimization of DISCO cleared sample preparation for mass spectrometry analysis
  - High-pH reversed-phase fractionation
  - Liquid chromatography and mass spectrometry (LC-MS)
- QUANTIFICATION AND STATISTICAL ANALYSIS
  - ClearMap quantification
  - Deep learning analyses
  - Proteomics data processing
  - Proteomics downstream data analysis
- ADDITIONAL RESOURCES

SUPPLEMENTAL INFORMATION

Supplemental information can be found online at https://doi.org/10.1016/j.cell.2022.11.021.

A video abstract is available at https://doi.org/10.1016/j.cell.2022.11.021#mmc9.

ACKNOWLEDGMENTS

A.-D.B. acknowledges support from the International Max Planck Research School for Life Sciences (IMPRS-LS). This work was supported by the Vascular Dementia Research Foundation, Deutsche Forschungsgemeinschaft (DFG, German Research Foundation) under Germany's Excellence Strategy within the framework of the Munich Cluster for Systems Neurology (EXC 2145 SyNergy, ID 390857198), the Bundesministerium für Bildung und Wissenschaft (BMBF) for Grant CLINSPECT-M (FKZ161L0214C, to S.F.L. and M.M.), ERC Consolidator Grant (AE, GA 865323), Nomis Heart Atlas Project Grant (Nomis Foundation), the Helmholtz AI program through grant Deeproad, and the Max Planck Society for the Advancement of Science. We thank our colleagues in the Department of Proteomics and Signal Transduction, Max Planck Institute of Biochemistry, for discussions and help. In particular, we thank I. Paron, A. Piras, and C. Deiml for technical support and J.B. Müller for column production. We thank Dr. Rupinder Kaur for her support. Some of the graphical illustrations used in the manuscript were prepared using BioRender.com. We thank Mr. Marin Bralo at iTERM for his technical support throughout this study.

AUTHOR CONTRIBUTIONS

A.E., M. Mann, H.S.B., and A.-D.B. conceptualized and designed the study. H.S.B., Z.R., and H.M. performed mice experiments, solvent-based organ clearing, light-sheet imaging procedures, and stitching of data. H.S.B. developed the LCM-based isolation procedure for target tissues from solvent-cleared organs. A.-D.B. developed the sample preparation workflow for proteomics analysis. A.-D.B., S.K., H.S.B., M. Molbay, and M.T. performed mass spectrometry-based proteomics analysis. R.A.-M., J.C.P., F.K., M.A., B.M., and F.T. developed deep learning models. M.A. and F.T. performed data analysis. M.I.T. performed atlas registration of 5xFAD brains. H.S.B. and D.K. performed ClearMAP analyses. A.E. conceptualized, and F.O. designed the robotic extraction system. Z.I.K. labeled, cleared, and imaged whole body of mouse. F.O., H.S.B., and S.K. extracted tissue from whole body and whole organs. S.K. performed mass spectrometry on robotic extracted samples. H.S.B. and S.K. analyzed the data. M.N., J.C.P., and A.D. performed 2D LCM registration to 3D data. S.M. and S.F.L. helped with the prototyping experiment. H.S.B., A.-D.B., M. Mann, and A.E. wrote the manuscript.

DECLARATION OF INTERESTS

F.T. reports receiving consulting fees from Roche Diagnostics GmbH and Cellarity, Inc., and ownership interest in Cellarity, Inc., and Dermagnostix. A.E.,

(F) The number of shared and unique set of proteins in cranium.
(G) Pearson correlation among cranium samples (n = 3 experimental replicates).
(H) Rank order of core protein abundance signals in cranium.
(I) Volcano plot showing the significantly enriched proteins in medial vs. lateral border of scapula.
(J) Heatmap showing the proteins related to innate immune system in medial vs. lateral border of scapula.
(K) Proteins related to adaptive immune system.
(L) Related to B cell receptor/T cell receptor pathway in scapula bone marrow niches.
See also Figure S7 and Video S6.

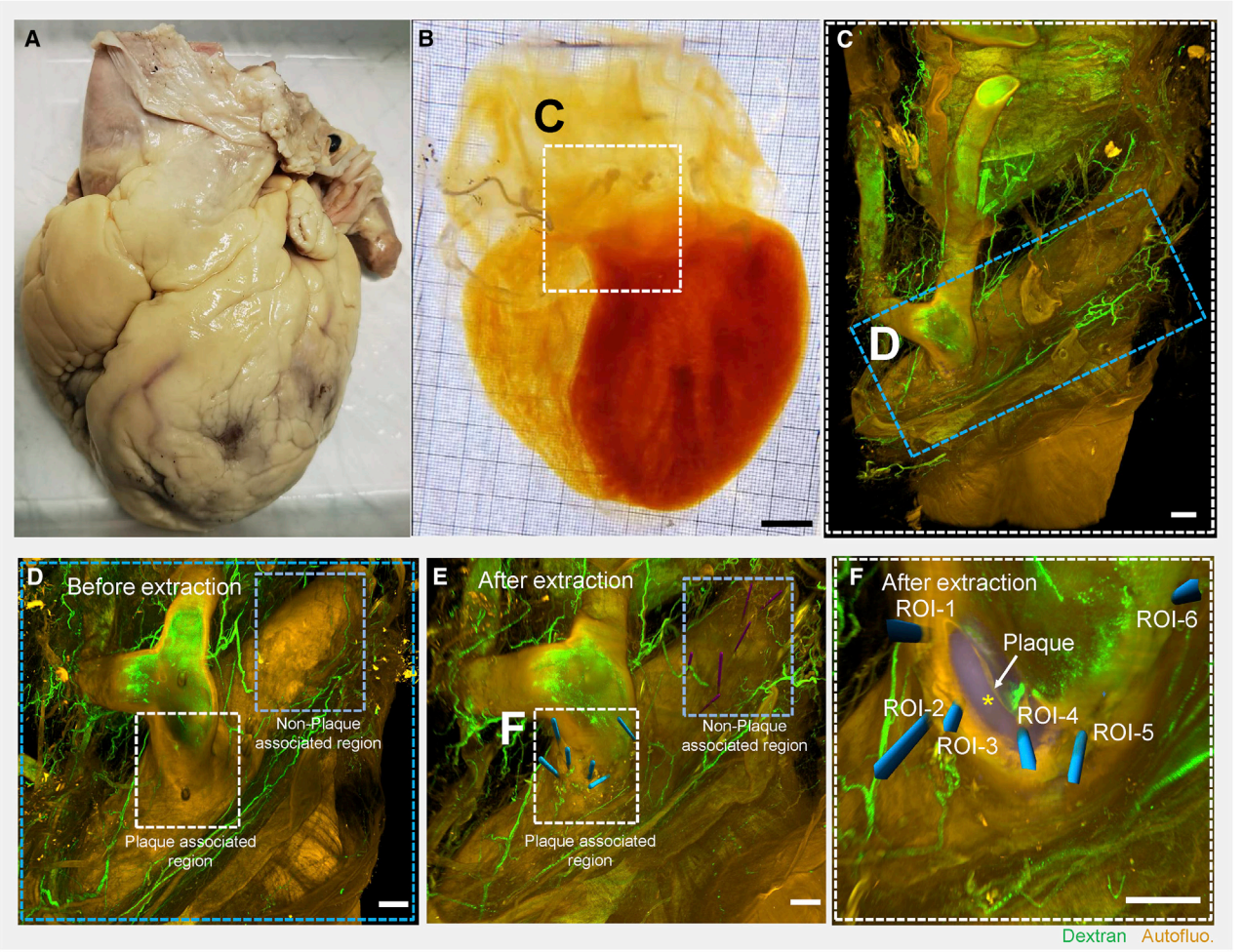

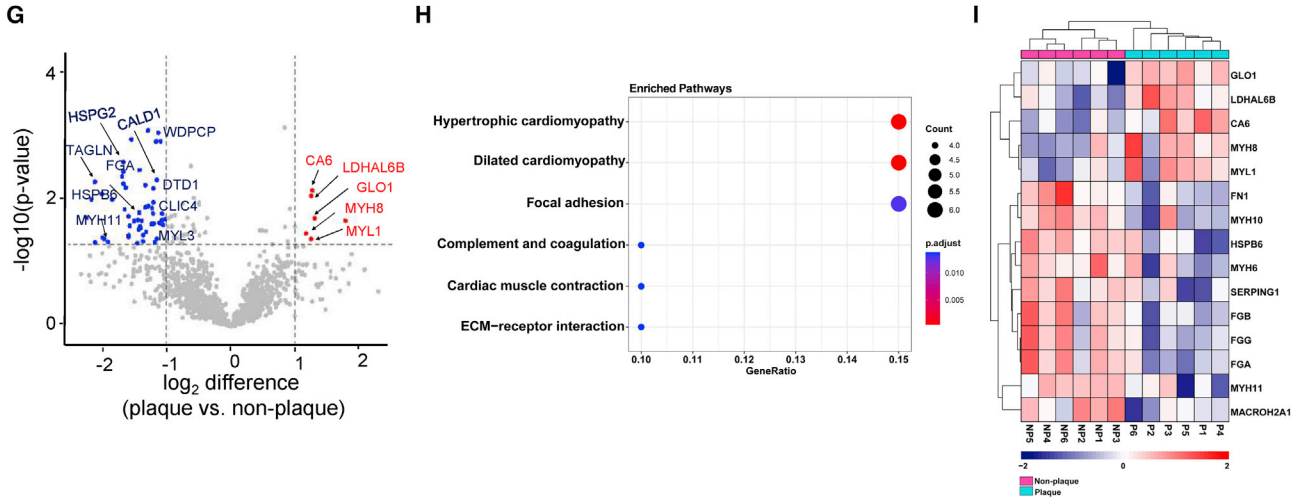

Figure 7. Human heart clearing, imaging, and proteomics from atherosclerotic plaques in coronary artery

(A) Image of whole human heart before clearing.

(B) Image of human heart after SHANEL clearing. Scale bar, 2 mm.

(C) 3D visualization of stiched images of portion of human heart showing dextran-labeled vessels (in green), plaques as autofluorescence (in gold). Scale bar, 1,000 μm.

(D) Stiched images of coronal artery with atherosclerotic plaque-associated regions and non-plaque regions before robotic guided extraction. Scale bar, 1,000 μm.

(legend continued on next page)

H.S.B., F.O., S.K., M.I.T., and M.N. have filed a patent related to robotics technologies presented in this work.

INCLUSION AND DIVERSITY

We support inclusive, diverse, and equitable conduct of research. We worked to ensure sex balance in the selection of non-human subjects. We worked to ensure diversity in experimental samples through the selection of the genomic datasets. One or more of the authors of this paper self-identifies as an underrepresented ethnic minority in their field of research or within their geographical location. One or more of the authors of this paper self-identifies as a gender minority in their field of research. One or more of the authors of this paper self-identifies as a member of the LGBTQIA+ community. We avoided "helicopter science" practices by including the participating local contributors from the region where we conducted the research as authors on the paper.

Received: May 3, 2021
Revised: June 13, 2022
Accepted: November 18, 2022
Published: December 22, 2022

REFERENCES

1. Braak, H., Thal, D.R., Ghebremedhin, E., and Del Tredici, K. (2011). Stages of the Pathologic Process in Alzheimer Disease: Age Categories From 1 to 100 Years. J. Neuropathol. Exp. Neurol. *70*, 960–969. https://doi.org/10.1097/NEN.0b013e318232a379.
2. Belle, M., Godefroy, D., Couly, G., Malone, S.A., Collier, F., Giacobini, P., and Chédotal, A. (2017). Tridimensional Visualization and Analysis of Early Human Development. Cell *169*, 161–173.e12. https://doi.org/10.1016/j.cell.2017.03.008.
3. Ueda, H.R., Ertürk, A., Chung, K., Gradinaru, V., Chédotal, A., Tomancak, P., and Keller, P.J. (2020). Tissue clearing and its applications in neuroscience. Nat. Rev. Neurosci. *21*, 61–79. https://doi.org/10.1038/s41583-019-0250-1.
4. Zhao, S., Todorov, M.I., Cai, R., -Maskari, R.A., Steinke, H., Kemter, E., Mai, H., Rong, Z., Warmer, M., Stanic, K., Schoppe, O., Paetzold, J.C., Gesierich, B., Wong, M.N., Huber, T.B., Duering, M., Bruns, O.T., Menze, B., Lipfert, J., Puelles, V.G., Wolf, E., Bechmann, I., and Erturk, A. (2020). Cellular and Molecular Probing of Intact Human Organs. Cell *180*, 796–812.e19. https://doi.org/10.1016/j.cell.2020.01.030.
5. Moen, E., Bannon, D., Kudo, T., Graf, W., Covert, M., and Van Valen, D. (2019). Deep learning for cellular image analysis. Nat. Methods *16*, 1233–1246. https://doi.org/10.1038/s41592-019-0403-1.
6. Sullivan, D.P., Winsnes, C.F., Åkesson, L., Hjelmare, M., Wiking, M., Schutten, R., Campbell, L., Leifsson, H., Rhodes, S., Nordgren, A., Smith, K., Revaz, B., Finnbogason, B., Szantner, A., and Lundberg, E. (2018). Deep learning is combined with massive-scale citizen science to improve large-scale image classification. Nat. Biotechnol. *36*, 820–828. https://doi.org/10.1038/nbt.4225.
7. Ji, A.L., Rubin, A.J., Thrane, K., Jiang, S., Reynolds, D.L., Meyers, R.M., Guo, M.G., George, B.M., Mollbrink, A., Bergenstråhle, J., Larsson, L., Bai, Y., Zhu, B., Bhaduri, A., Meyers, J.M., Rovira-Clave, X., Hollmig, S.T., Aasi, S.Z., Nolan, G.P., Lundeberg, J., and Khavari, P.A. (2020). Multimodal Analysis of Composition and Spatial Architecture in Human Squamous Cell Carcinoma. Cell *182*, 497–514.e22. https://doi.org/10.1016/j.cell.2020.05.039.
8. Stuart, T., and Satija, R. (2019). Integrative single-cell analysis. Nat. Rev. Genet. *20*, 257–272. https://doi.org/10.1038/s41576-019-0093-7.
9. VanHorn, S., and Morris, S.A. (2021). Next-Generation Lineage Tracing and Fate Mapping to Interrogate Development. Dev. Cell *56*, 7–21. https://doi.org/10.1016/j.devcel.2020.10.021.
10. Brunner, A.D., Thielert, M., Vasilopoulou, C., Ammar, C., Coscia, F., Mund, A., Hoerning, O.B., Bache, N., Apalategui, A., Lubeck, M., Richter, S., Fischer, D.S., Raether, O., Park, M.A., Meier, F., Theis, F.J., and Mann, M. (2022). Ultra-high sensitivity mass spectrometry quantifies single-cell proteome changes upon perturbation. Mol. Syst. Biol. *18*, e10798. https://doi.org/10.15252/msb.202110798.
11. Reimegård, J., Tarbier, M., Danielsson, M., Schuster, J., Baskaran, S., Panagiotou, S., Dahl, N., Friedländer, M.R., and Gallant, C.J. (2021). A combined approach for single-cell mRNA and intracellular protein expression analysis. Commun Biol *4*, 624. https://doi.org/10.1038/s42003-021-02142-w.
12. Johnson, E.C.B., Carter, E.K., Dammer, E.B., Duong, D.M., Gerasimov, E.S., Liu, Y., Liu, J., Betarbet, R., Ping, L., Yin, L., Serrano, G.E., Beach, T.G., Peng, J., De Jager, P.L., Haroutunian, V., Zhang, B., Gaiteri, C., Bennett, D.A., Gearing, M., Wingo, T.S., Wingo, A.P., Lah, J.J., Levey, A.I., and Seyfried, N.T. (2022). Large-scale deep multi-layer analysis of Alzheimer's disease brain reveals strong proteomic disease-related changes not observed at the RNA level. Nat. Neurosci. *25*, 213–225. https://doi.org/10.1038/s41593-021-00999-y.
13. Wegler, C., Ölander, M., Wiśniewski, J.R., Lundquist, P., Zettl, K., Åsberg, A., Hjelmesæth, J., Andersson, T.B., and Artursson, P. (2020). Global variability analysis of mRNA and protein concentrations across and within human tissues. NAR Genom Bioinform *2*, lqz010. https://doi.org/10.1093/nargab/lqz010.
14. Budnik, B., Levy, E., Harmange, G., and Slavov, N. (2018). SCoPE-MS: mass spectrometry of single mammalian cells quantifies proteome heterogeneity during cell differentiation. Genome Biol. *19*, 161. https://doi.org/10.1186/s13059-018-1547-5.
15. Cheung, T.K., Lee, C.-Y., Bayer, F.P., McCoy, A., Kuster, B., and Rose, C.M. (2021). Defining the carrier proteome limit for single-cell proteomics. Nat. Methods *18*, 76–83. https://doi.org/10.1038/s41592-020-01002-5.
16. Cong, Y., Motamedchaboki, K., Misal, S.A., Liang, Y., Guise, A.J., Truong, T., Huguet, R., Plowey, E.D., Zhu, Y., Lopez-Ferrer, D., et al. (2021). Ultrasensitive single-cell proteomics workflow identifies >1000 protein groups per mammalian cell. Chem. Sci. *12*, 1001–1006. https://doi.org/10.1039/D0SC03636F.
17. Mund, A., Coscia, F., Kriston, A., Hollandi, R., Kovács, F., Brunner, A.-D., Migh, E., Schweizer, L., Santos, A., Bzorek, M., Naimy, S., Rahbek-Gjerdrum, L.M., Dyring-Andersen, B., Bulkescher, J., Lukas, C., Eckert, M.A., Lengyel, E., Gnann, C., Lundberg, E., Horvath, P., and Mann, M. (2022). Deep Visual Proteomics defines single-cell identity and heterogeneity. Nat. Biotechnol. *40*, 1231–1240. https://doi.org/10.1038/s41587-022-01302-5.
18. Alon, S., Goodwin, D.R., Sinha, A., Wassie, A.T., Chen, F., Daugharthy, E.R., Bando, Y., Kajita, A., Xue, A.G., Marrett, K., Prior, R., Cui, Y., Payne, A.C., Yao, C.C., Suk, H.J., Wang, R., Yu, C.C.J., Tillberg, P., Reginato, P., Pak, N., Liu, S., Punthambaker, S., Iyer, E.P.R., Kohman, R.E., Miller, J.A., Lein, E.S., Lako, A., Cullen, N., Rodig, S., Helvie, K., Abravanel, D.L., Wagle, N., Johnson, B.E., Klughammer, J., Slyper, M., Waldman, J., Jane-Valbuena, J., Rozenblatt-Rosen, O., Regev, A., IMAXT Consortium, Church, G.M., Marblestone, A.H., Boyden, E.S., Al Sa'd, M., Alon, S.,

(E) Stiched images of coronary artery after extraction of ROIs, extraction points are shown in blue (plaque region) and in magenta (non-plaque region). Scale bar, 1,000 μm.
(F) Enlarged view of ROIs around the segmented plaque marked in (E). Scale bar, 1,000 μm.
(G) Volcano plot showing the significantly enriched proteins in plaque (ROIs 1–6) vs. non-plaque areas.
(H) Pathway enrichment of differentially regulated proteins.
(I) Heatmap of differentially regulated proteins in each ROIs.
See also Figure S7 and Video S7.

Aparicio, S., Battistoni, G., Balasubramanian, S., Becker, R., Bodenmiller, B., Boyden, E.S., Bressan, D., Bruna, A., Burger, M., Caldas, C., Callari, M., Cannell, I.G., Casbolt, H., Chornay, N., Cui, Y., Dariush, A., Dinh, K., Emenari, A., Eyal-Lubling, Y., Fan, J., Fatemi, A., Fisher, E., Gonzalez-Solares, E.A., Gonzalez-Fernandez, C., Goodwin, D., Greenwood, W., Grimaldi, F., Hannon, G.J., Harris, O., Harris, S., Jauset, C., Joyce, J.A., Karagiannis, E.D., Kovacevic, T., Kuett, L., Kunes, R., Kupcu Yoldas, A., Lai, D., Laks, E., Lee, H., Lee, M., Lerda, G., Li, Y., McPherson, A., Millar, N., Mulvey, C.M., Nugent, F., O'Flanagan, C.H., Paez-Ribes, M., Pearsall, I., Qosaj, F., Roth, A.J., Rueda, O.M., Ruiz, T., Sawicka, K., Sepulveda, L.A., Shah, S.P., Shea, A., Sinha, A., Smith, A., Tavare, S., Tietscher, S., Vazquez-Garcia, I., Vogl, S.L., Walton, N.A., Wassie, A.T., Watson, S.S., Weselak, J., Wild, S.A., Williams, E., Windhager, J., Whitmarsh, T., Xia, C., Zheng, P., and Zhuang, X. (2021). Expansion sequencing: Spatially precise in situ transcriptomics in intact biological systems. Science *371*, eaax2656. https://doi.org/10.1126/science.aax2656.

19. van den Brink, S.C., Alemany, A., van Batenburg, V., Moris, N., Blotenburg, M., Vivié, J., Baillie-Johnson, P., Nichols, J., Sonnen, K.F., Martinez Arias, A., and van Oudenaarden, A. (2020). Single-cell and spatial transcriptomics reveal somitogenesis in gastruloids. Nature *582*, 405–409. https://doi.org/10.1038/s41586-020-2024-3.

20. Chen, W.-T., Lu, A., Craessaerts, K., Pavie, B., Sala Frigerio, C., Corthout, N., Qian, X., Laláková, J., Kühnemund, M., Voytyuk, I., Wolfs, L., Mancuso, R., Salta, E., Balusu, S., Snellinx, A., Munck, S., Jurek, A., Fernandez Navarro, J., Saido, T.C., Huitinga, I., Lundeberg, J., Fiers, M., and De Strooper, B. (2020). Spatial Transcriptomics and In Situ Sequencing to Study Alzheimer's Disease. Cell *182*, 976–991.e19. https://doi.org/10.1016/j.cell.2020.06.038.

21. Liu, Y., Yang, M., Deng, Y., Su, G., Enninful, A., Guo, C.C., Tebaldi, T., Zhang, D., Kim, D., Bai, Z., Norris, E., Pan, A., Li, J., Xiao, Y., Halene, S., and Fan, R. (2020). High-Spatial-Resolution Multi-Omics Sequencing via Deterministic Barcoding in Tissue. Cell *183*, 1665–1681.e18. https://doi.org/10.1016/j.cell.2020.10.026.

22. Mahdessian, D., Cesnik, A.J., Gnann, C., Danielsson, F., Stenström, L., Arif, M., Zhang, C., Le, T., Johansson, F., Schutten, R., Backstrom, A., Axelsson, U., Thul, P., Cho, N.H., Carja, O., Uhlen, M., Mardinoglu, A., Stadler, C., Lindskog, C., Ayoglu, B., Leonetti, M.D., Ponten, F., Sullivan, D.P., and Lundberg, E. (2021). Spatiotemporal dissection of the cell cycle with single-cell proteogenomics. Nature *590*, 649–654. https://doi.org/10.1038/s41586-021-03232-9.

23. Rodriques, S.G., Stickels, R.R., Goeva, A., Martin, C.A., Murray, E., Vanderburg, C.R., Welch, J., Chen, L.M., Chen, F., and Macosko, E.Z. (2019). Slide-seq: A scalable technology for measuring genome-wide expression at high spatial resolution. Science *363*, 1463–1467. https://doi.org/10.1126/science.aaw1219.

24. Ståhl, P.L., Salmén, F., Vickovic, S., Lundmark, A., Navarro, J.F., Magnusson, J., Giacomello, S., Asp, M., Westholm, J.O., Huss, M., Mollbrink, A., Linnarsson, S., Codeluppi, S., Borg, A., Ponten, F., Costea, P.I., Sahlen, P., Mulder, J., Bergmann, O., Lundeberg, J., and Frisen, J. (2016). Visualization and analysis of gene expression in tissue sections by spatial transcriptomics. Science *353*, 78–82. https://doi.org/10.1126/science.aaf2403.

25. Takei, Y., Yun, J., Zheng, S., Ollikainen, N., Pierson, N., White, J., Shah, S., Thomassie, J., Suo, S., Eng, C.-H.L., Guttman, M., Yuan, G.C., and Cai, L. (2021). Integrated spatial genomics reveals global architecture of single nuclei. Nature *590*, 344–350. https://doi.org/10.1038/s41586-020-03126-2.

26. Giesen, C., Wang, H.A.O., Schapiro, D., Zivanovic, N., Jacobs, A., Hattendorf, B., Schüffler, P.J., Grolimund, D., Buhmann, J.M., Brandt, S., Varga, Z., Wild, P.J., Gunther, D., and Bodenmiller, B. (2014). Highly multiplexed imaging of tumor tissues with subcellular resolution by mass cytometry. Nat. Methods *11*, 417–422. https://doi.org/10.1038/nmeth.2869.

27. Ko, J., Wilkovitsch, M., Oh, J., Kohler, R.H., Bolli, E., Pittet, M.J., Vinegoni, C., Sykes, D.B., Mikula, H., Weissleder, R., and Carlson, J.C.T. (2022). Spatiotemporal multiplexed immunofluorescence imaging of living cells and tissues with bioorthogonal cycling of fluorescent probes. Nat. Biotechnol. *40*, 1654–1662. https://doi.org/10.1038/s41587-022-01339-6.

28. Goltsev, Y., Samusik, N., Kennedy-Darling, J., Bhate, S., Hale, M., Vazquez, G., Black, S., and Nolan, G.P. (2018). Deep Profiling of Mouse Splenic Architecture with CODEX Multiplexed Imaging. Cell *174*, 968–981.e15. https://doi.org/10.1016/j.cell.2018.07.010.

29. Saka, S.K., Wang, Y., Kishi, J.Y., Zhu, A., Zeng, Y., Xie, W., Kirli, K., Yapp, C., Cicconet, M., Beliveau, B.J., Lapan, S.W., Yin, S., Lin, M., Boyden, E.S., Kaeser, P.S., Pihan, G., Church, G.M., and Yin, P. (2019). Immuno-SABER enables highly multiplexed and amplified protein imaging in tissues. Nat. Biotechnol. *37*, 1080–1090. https://doi.org/10.1038/s41587-019-0207-y.

30. Radtke, A.J., Kandov, E., Lowekamp, B., Speranza, E., Chu, C.J., Gola, A., Thakur, N., Shih, R., Yao, L., Yaniv, Z.R., Beuschel, R.T., Kabat, J., Croteau, J., Davis, J., Hernandez, J.M., and Germain, R.N. (2020). IBEX: A versatile multiplex optical imaging approach for deep phenotyping and spatial analysis of cells in complex tissues. Proc. Natl. Acad. Sci. USA. *117*, 33455–33465. https://doi.org/10.1073/pnas.2018488117.

31. Ueda, H.R., Dodt, H.-U., Osten, P., Economo, M.N., Chandrashekar, J., and Keller, P.J. (2020). Whole-Brain Profiling of Cells and Circuits in Mammals by Tissue Clearing and Light-Sheet Microscopy. Neuron *106*, 369–387. https://doi.org/10.1016/j.neuron.2020.03.004.

32. Aebersold, R., and Mann, M. (2016). Mass-spectrometric exploration of proteome structure and function. Nature *537*, 347–355. https://doi.org/10.1038/nature19949.

33. Richardson, D.S., Guan, W., Matsumoto, K., Pan, C., Chung, K., Ertürk, A., Ueda, H.R., and Lichtman, J.W. (2021). TISSUE CLEARING. Nat Rev Methods Primers *1*, 84. https://doi.org/10.1038/s43586-021-00080-9.

34. Cai, R., Pan, C., Ghasemigharagoz, A., Todorov, M.I., Förstera, B., Zhao, S., Bhatia, H.S., Parra-Damas, A., Mrowka, L., Theodorou, D., Rempfler, M., Xavier, A.L.R., Kress, B.T., Benakis, C., Steinke, H., Liebscher, S., Bechmann, I., Liesz, A., Menze, B., Kerschensteiner, M., Nedergaard, M., and Erturk, A. (2019). Panoptic imaging of transparent mice reveals whole-body neuronal projections and skull-meninges connections. Nat. Neurosci. *22*, 317–327. https://doi.org/10.1038/s41593-018-0301-3.

35. Langlois, J.A., Rutland-Brown, W., and Thomas, K.E. (2005). The incidence of traumatic brain injury among children in the United States: differences by race. J. Head Trauma Rehabil. *20*, 229–238. https://doi.org/10.1097/00001199-200505000-00006.

36. Ertürk, A., Mentz, S., Stout, E.E., Hedehus, M., Dominguez, S.L., Neumaier, L., Krammer, F., Llovera, G., Srinivasan, K., Hansen, D.V., Liesz, A., Scearce-Levie, K.A., and Sheng, M. (2016). Interfering with the Chronic Immune Response Rescues Chronic Degeneration After Traumatic Brain Injury. J. Neurosci. *36*, 9962–9975. https://doi.org/10.1523/JNEUROSCI.1898-15.2016.

37. Renier, N., Adams, E.L., Kirst, C., Wu, Z., Azevedo, R., Kohl, J., Autry, A.E., Kadiri, L., Umadevi Venkataraju, K., Zhou, Y., Wang, V.X., Tang, C.Y., Olsen, O., Dulac, C., Osten, P., and Tessier-Lavigne, M. (2016). Mapping of Brain Activity by Automated Volume Analysis of Immediate Early Genes. Cell *165*, 1789–1802. https://doi.org/10.1016/j.cell.2016.05.007.

38. Chen, M., Song, H., Cui, J., Johnson, C.E., Hubler, G.K., DePalma, R.G., Gu, Z., and Xia, W. (2018). Proteomic Profiling of Mouse Brains Exposed to Blast-Induced Mild Traumatic Brain Injury Reveals Changes in Axonal Proteins and Phosphorylated Tau. J Alzheimers Dis *66*, 751–773. https://doi.org/10.3233/JAD-180726.

39. Asher, R.A., Morgenstern, D.A., Fidler, P.S., Adcock, K.H., Oohira, A., Braistead, J.E., Levine, J.M., Margolis, R.U., Rogers, J.H., and Fawcett, J.W. (2000). Neurocan is upregulated in injured brain and in cytokine-treated astrocytes. J. Neurosci. *20*, 2427–2438. https://doi.org/10.1523/jneurosci.20-07-02427.2000.

40. Alaamery, M., Albesher, N., Aljawini, N., Alsuwailm, M., Massadeh, S., Wheeler, M.A., Chao, C., and Quintana, F.J. (2021). Role of sphingolipid metabolism in neurodegeneration. J. Neurochem. *158*, 25–35. https://doi.org/10.1111/jnc.15044.

41. Gebai, A., Gorelik, A., Li, Z., Illes, K., and Nagar, B. (2018). Structural basis for the activation of acid ceramidase. Nat. Commun. *9*, 1621. https://doi.org/10.1038/s41467-018-03844-2.

42. Parveen, F., Bender, D., Law, S.-H., Mishra, V.K., Chen, C.-C., and Ke, L.-Y. (2019). Role of Ceramidases in Sphingolipid Metabolism and Human Diseases. Cells *8*, E1573. https://doi.org/10.3390/cells8121573.

43. Kyriakou, K., W Lederer, C., Kleanthous, M., Drousiotou, A., and Malekkou, A. (2020). Acid Ceramidase Depletion Impairs Neuronal Survival and Induces Morphological Defects in Neurites Associated with Altered Gene Transcription and Sphingolipid Content. Int. J. Mol. Sci. *21*, E1607. https://doi.org/10.3390/ijms21051607.

44. Rumyantseva, A., Popovic, M., and Trifunovic, A. (2022). CLPP deficiency ameliorates neurodegeneration caused by impaired mitochondrial protein synthesis. Brain *145*, 92–104. https://doi.org/10.1093/brain/awab303.

45. Shi, Y., Yi, C., Li, X., Wang, J., Zhou, F., and Chen, X. (2017). Overexpression of Mitofusin2 decreased the reactive astrocytes proliferation in vitro induced by oxygen-glucose deprivation/reoxygenation. Neurosci. Lett. *639*, 68–73. https://doi.org/10.1016/j.neulet.2016.12.052.

46. Meyer-Luehmann, M., Spires-Jones, T.L., Prada, C., Garcia-Alloza, M., de Calignon, A., Rozkalne, A., Koenigsknecht-Talboo, J., Holtzman, D.M., Bacskai, B.J., and Hyman, B.T. (2008). Rapid appearance and local toxicity of amyloid-beta plaques in a mouse model of Alzheimer's disease. Nature *451*, 720–724. https://doi.org/10.1038/nature06616.

47. Ronneberger, O., Fischer, P., and Brox, T. (2015). U-Net: Convolutional Networks for Biomedical Image Segmentation. https://doi.org/10.48550/arXiv.1505.04597.

48. Todorov, M.I., Paetzold, J.C., Schoppe, O., Tetteh, G., Shit, S., Efremov, V., Todorov-Völgyi, K., Düring, M., Dichgans, M., Piraud, M., Menze, B., and Erturk, A. (2020). Machine learning analysis of whole mouse brain vasculature. Nat. Methods *17*, 442–449. https://doi.org/10.1038/s41592-020-0792-1.

49. Wang, Q., Ding, S.-L., Li, Y., Royall, J., Feng, D., Lesnar, P., Graddis, N., Naeemi, M., Facer, B., Ho, A., Dolbeare, T., Blanchard, B., Dee, N., Wakeman, W., Hirokawa, K.E., Szafer, A., Sunkin, S.M., Oh, S.W., Bernard, A., Phillips, J.W., Hawrylycz, M., Koch, C., Zeng, H., Harris, J.A., and Ng, L. (2020). The Allen Mouse Brain Common Coordinate Framework: A 3D Reference Atlas. Cell *181*, 936–953.e20. https://doi.org/10.1016/j.cell.2020.04.007.

50. Claudi, F., Tyson, A.L., Petrucco, L., Margrie, T.W., Portugues, R., and Branco, T. (2021). Visualizing anatomically registered data with brainrender. Elife *10*, e65751. https://doi.org/10.7554/eLife.65751.

51. Lichtenthaler, S.F. (2006). Ectodomain shedding of the amyloid precursor protein: cellular control mechanisms and novel modifiers. Neurodegener. Dis. *3*, 262–269. https://doi.org/10.1159/000095265.

52. Meckelein, B., de Silva, H., Roses, A.D., Rao, P., Pettenati, M.J., Xu, P.T., Hodge, R., Glucksman, M.J., and Abraham, C.R. (1996). Human endopeptidase (THOP1) is localized on chromosome 19 within the linkage region for the late-onset alzheimer disease AD2 locus. Genomics *31*, 246–249. https://doi.org/10.1006/geno.1996.0041.

53. Pollio, G., Hoozemans, J.J., Andersen, C.A., Roncarati, R., Rosi, M.C., van Haastert, E.S., Seredenina, T., Diamanti, D., Gotta, S., Fiorentini, A., Magnoni, L., Raggiaschi, R., Rozemuller, A.J., Casamenti, F., Caricasole, A., and Terstappen, G.C. (2008). Increased expression of the oligopeptidase THOP1 is a neuroprotective response to Aβ toxicity. Neurobiol. Dis. *31*, 145–158. https://doi.org/10.1016/j.nbd.2008.04.004.

54. Xu, S., Di, Z., He, Y., Wang, R., Ma, Y., Sun, R., Li, J., Wang, T., Shen, Y., Fang, S., Feng, L., and Shen, Y. (2019). Mesencephalic astrocyte-derived neurotrophic factor (MANF) protects against Aβ toxicity via attenuating Aβ-induced endoplasmic reticulum stress. J. Neuroinflammation *16*, 35. https://doi.org/10.1186/s12974-019-1429-0.

55. Arisi, I., D'Onofrio, M., Brandi, R., Felsani, A., Capsoni, S., Drovandi, G., Felici, G., Weitschek, E., Bertolazzi, P., and Cattaneo, A. (2011). Gene expression biomarkers in the brain of a mouse model for Alzheimer's disease: mining of microarray data by logic classification and feature selection. J Alzheimers Dis *24*, 721–738. https://doi.org/10.3233/JAD-2011-101881.

56. Marom, R., Jain, M., Burrage, L.C., Song, I.-W., Graham, B.H., Brown, C.W., Stevens, S.J., Stegmann, A.P., Gunter, A.T., Kaplan, J.D., Gavrilova, R.H., Shinawi, M., Rosenfeld, J.A., Bae, Y., Tran, A.A., Chen, Y., Lu, J.T., Gibbs, R.A., Eng, C., Yang, Y., Rousseau, J., de Vries, B.B., Campeau, P.M., and Lee, B. (2017). Heterozygous variants in ACTL6A, encoding a component of the BAF complex, are associated with intellectual disability. Hum. Mutat. *38*, 1365–1371. https://doi.org/10.1002/humu.23282.

57. Depp, C., Sun, T., Sasmita, A.O., Spieth, L., Berghoff, S.A., Steixner-Kumar, A.A., Subramanian, S., Möbius, W., Göbbels, S., Saher, G., Zampar, S., Wirths, O., Thalmann, M., Saito, T., Saido, T., Krueger-Burg, D., Kawaguchi, R., Willem, M., Haass, C., Geschwind, D., Ehrenreich, H., Stassart, R., and Nave, K.A. (2021). Ageing-associated myelin dysfunction drives amyloid deposition in mouse models of Alzheimer's disease. https://doi.org/10.1101/2021.07.31.454562.

58. Kolabas, Z.I., Kuemmerle, L.B., Perneczky, R., Förstera, B., Büttner, M., Caliskan, O.S., Ali, M., Rong, Z., Mai, H., Hummel, S., Bartos, L.M., Biechele, G., Zatcepin, A., Albert, N.L., Unterrainer, M., Gnorich, J., Zhao, S., Khalin, I., Rauchmann, B.S., Molbay, M., Sterr, M., Kunze, I., Stanic, K., Besson-Girard, S., Kopczak, A., Katzdobler, S., Palleis, C., Gokce, O., Lickert, H., Steinke, H., Bechmann, I., Buerger, K., Levin, J., Haass, C., Dichgans, M., Havla, J., Kumpfel, T., Kerschensteiner, M., Simons, M., Plesnila, N., Krahmer, N., Bhatia, H.S., Erener, S., Hellal, F., Brendel, M., Theis, F.J., and Erturk, A. (2021). Multi-omics and 3D-imaging reveal bone heterogeneity and unique calvaria cells in neuroinflammation. https://doi.org/10.1101/2021.12.24.473988.

59. Nabel, E.G., and Braunwald, E. (2012). A tale of coronary artery disease and myocardial infarction. N. Engl. J. Med. *366*, 54–63. https://doi.org/10.1056/NEJMra1112570.

60. Wong, N.D. (2014). Epidemiological studies of CHD and the evolution of preventive cardiology. Nat. Rev. Cardiol. *11*, 276–289. https://doi.org/10.1038/nrcardio.2014.26.

61. Fernandez, D.M., Rahman, A.H., Fernandez, N.F., Chudnovskiy, A., Amir, E.-A.D., Amadori, L., Khan, N.S., Wong, C.K., Shamailova, R., Hill, C.A., Wang, Z., Remark, R., Li, J.R., Pina, C., Faries, C., Awad, A.J., Moss, N., Bjorkegren, J.L.M., Kim-Schulze, S., Gnjatic, S., Ma'ayan, A., Mocco, J., Faries, P., Merad, M., and Giannarelli, C. (2019). Single-cell immune landscape of human atherosclerotic plaques. Nat Med *25*, 1576–1588. https://doi.org/10.1038/s41591-019-0590-4.

62. Litviňuková, M., Talavera-López, C., Maatz, H., Reichart, D., Worth, C.L., Lindberg, E.L., Kanda, M., Polanski, K., Heinig, M., Lee, M., Nadelmann, E.R., Roberts, K., Tuck, L., Fasouli, E.S., DeLaughter, D.M., McDonough, B., Wakimoto, H., Gorham, J.M., Samari, S., Mahbubani, K.T., Saeb-Parsy, K., Patone, G., Boyle, J.J., Zhang, H., Zhang, H., Viveiros, A., Oudit, G.Y., Bayraktar, O.A., Seidman, J.G., Seidman, C.E., Noseda, M., Hubner, N., and Teichmann, S.A. (2020). Cells of the adult human heart. Nature *588*, 466–472. https://doi.org/10.1038/s41586-020-2797-4.

63. Meng, L.B., Li, J.Y., Xu, H.X., Wu, D.S., Shan, M.J., Chen, Y.H., Xu, J.P., Liu, L.T., Chen, Z., Li, Y.J., Gong, T., and Liu, D. (2022). A potential biomarker for clinical atherosclerosis: A novel insight derived from myosin heavy chain 10 promoting transformation of vascular smooth muscle cells. Clin. Transl. Med. *12*, e672. https://doi.org/10.1002/ctm2.672.

64. Takahashi, L., Ishigami, T., Tomiyama, H., Kato, Y., Kikuchi, H., Tasaki, K., Yamashita, J., Inoue, S., Taguri, M., Nagao, T., Chikamori, T., Ishikawa, Y., and Yokoyama, U. (2021). Increased Plasma Levels of Myosin Heavy Chain 11 Is Associated with Atherosclerosis. J. Clin. Med. *10*, 3155. https://doi.org/10.3390/jcm10143155.

65. Mäkinen, V.-P., Civelek, M., Meng, Q., Zhang, B., Zhu, J., Levian, C., Huan, T., Segrè, A.V., Ghosh, S., Vivar, J., Nikpay, M., Stewart, A.F.R., Nelson, C.P., Willenborg, C., Erdmann, J., Blakenberg, S., O'Donnell, C.J., Marz, W., Laaksonen, R., Epstein, S.E., Kathiresan, S., Shah, S.H., Hazen, S.L., Reilly, M.P., Lusis, A.J., Samani, N.J., Schunkert, H., Quertermous, T., McPherson, R., Yang, X., and Assimes, T.L. (2014). Integrative genomics reveals novel molecular pathways and gene networks for coronary

artery disease. PLoS Genet. *10*, e1004502. https://doi.org/10.1371/journal.pgen.1004502.

66. Adeva-Andany, M.M., Fernández-Fernández, C., Sánchez-Bello, R., Donapetry-García, C., and Martínez-Rodríguez, J. (2015). The role of carbonic anhydrase in the pathogenesis of vascular calcification in humans. Atherosclerosis *241*, 183–191. https://doi.org/10.1016/j.atherosclerosis.2015.05.012.
67. Yuan, L., Wang, M., Liu, T., Lei, Y., Miao, Q., Li, Q., Wang, H., Zhang, G., Hou, Y., and Chang, X. (2019). Carbonic Anhydrase 1-Mediated Calcification Is Associated With Atherosclerosis, and Methazolamide Alleviates Its Pathogenesis. Front. Pharmacol. *10*, 766. https://doi.org/10.3389/fphar.2019.00766.
68. Robichaud, S., Fairman, G., Vijithakumar, V., Mak, E., Cook, D.P., Pelletier, A.R., Huard, S., Vanderhyden, B.C., Figeys, D., Lavallée-Adam, M., Baetz, K., and Ouimet, M. (2021). Identification of novel lipid droplet factors that regulate lipophagy and cholesterol efflux in macrophage foam cells. Autophagy *17*, 3671–3689. https://doi.org/10.1080/15548627.2021.1886839.
69. Whitesell, J.D., Buckley, A.R., Knox, J.E., Kuan, L., Graddis, N., Pelos, A., Mukora, A., Wakeman, W., Bohn, P., Ho, A., Hirokawa, K.E., and Harris, J.A. (2019). Whole brain imaging reveals distinct spatial patterns of amyloid beta deposition in three mouse models of Alzheimer's disease. J. Comp. Neurol. *527*, 2122–2145. https://doi.org/10.1002/cne.24555.
70. Oddo, S., Caccamo, A., Shepherd, J.D., Murphy, M., Golde, T.E., Kayed, R., Metherate, R., Mattson, M.P., Akbari, Y., and LaFerla, F.M. (2003). Triple-transgenic model of Alzheimer's disease with plaques and tangles: intracellular Abeta and synaptic dysfunction. Neuron *39*, 409–421. https://doi.org/10.1016/S0896-6273(03)00434-3.
71. Bai, B., Wang, X., Li, Y., Chen, P.-C., Yu, K., Dey, K.K., Yarbro, J.M., Han, X., Lutz, B.M., Rao, S., Jiao, Y., Sifford, J.M., Han, J., Wang, M., Tan, H., Shaw, T.I., Cho, J.H., Zhou, S., Wang, H., Niu, M., Mancieri, A., Messler, K.A., Sun, X., Wu, Z., Pagala, V., High, A.A., Bi, W., Zhang, H., Chi, H., Haroutunian, V., Zhang, B., Beach, T.G., Yu, G., and Peng, J. (2020). Deep Multilayer Brain Proteomics Identifies Molecular Networks in Alzheimer's Disease Progression. Neuron *105*, 975–991.e7. https://doi.org/10.1016/j.neuron.2019.12.015.
72. Kim, D.K., Han, D., Park, J., Choi, H., Park, J.-C., Cha, M.-Y., Woo, J., Byun, M.S., Lee, D.Y., Kim, Y., and Mook-Jung, I. (2019). Deep proteome profiling of the hippocampus in the 5XFAD mouse model reveals biological process alterations and a novel biomarker of Alzheimer's disease. Exp. Mol. Med. *51*, 1–17. https://doi.org/10.1038/s12276-019-0326-z.
73. Neuner, S.M., Wilmott, L.A., Hoffmann, B.R., Mozhui, K., and Kaczorowski, C.C. (2017). Hippocampal proteomics defines pathways associated with memory decline and resilience in normal aging and Alzheimer's disease mouse models. Behav. Brain Res. *322*, 288–298. https://doi.org/10.1016/j.bbr.2016.06.002.
74. Boza-Serrano, A., Yang, Y., Paulus, A., and Deierborg, T. (2018). Innate immune alterations are elicited in microglial cells before plaque deposition in the Alzheimer's disease mouse model 5xFAD. Sci. Rep. *8*, 1550. https://doi.org/10.1038/s41598-018-19699-y.
75. Rangaraju, S., Dammer, E.B., Raza, S.A., Rathakrishnan, P., Xiao, H., Gao, T., Duong, D.M., Pennington, M.W., Lah, J.J., Seyfried, N.T., and Levey, A.I. (2018). Identification and therapeutic modulation of a pro-inflammatory subset of disease-associated-microglia in Alzheimer's disease. Mol Neurodegeneration *13*, 24. https://doi.org/10.1186/s13024-018-0254-8.
76. Gail Canter, R., Huang, W.-C., Choi, H., Wang, J., Ashley Watson, L., Yao, C.G., Abdurrob, F., Bousleiman, S.M., Young, J.Z., Bennett, D.A., Delalle, I., Chung, K., and Tsai, L.H. (2019). 3D mapping reveals network-specific amyloid progression and subcortical susceptibility in mice. Commun Biol *2*, 360. https://doi.org/10.1038/s42003-019-0599-8.
77. Oblak, A.L., Lin, P.B., Kotredes, K.P., Pandey, R.S., Garceau, D., Williams, H.M., Uyar, A., O'Rourke, R., O'Rourke, S., Ingraham, C., Bednarczyk, D., Belanger, M., Cope, Z.A., Little, G.J., Williams, S.P.G., Ash, C., Bleckert, A., Ragan, T., Logsdon, B.A., Mangravite, L.M., Sukoff Rizzo, S.J., Territo, P.R., Carter, G.W., Howell, G.R., Sasner, M., and Lamb, B.T. (2021). Comprehensive Evaluation of the 5XFAD Mouse Model for Preclinical Testing Applications: A MODEL-AD Study. Front. Aging Neurosci. *13*, 713726. https://doi.org/10.3389/fnagi.2021.713726.
78. Percie du Sert, N., Hurst, V., Ahluwalia, A., Alam, S., Avey, M.T., Baker, M., Browne, W.J., Clark, A., Cuthill, I.C., Dirnagl, U., Emerson, M., Garner, P., Holgate, S.T., Howells, D.W., Karp, N.A., Lazic, S.E., Lidster, K., MacCallum, C.J., Macleod, M., Pearl, E.J., Petersen, O.H., Rawle, F., Reynolds, P., Rooney, K., Sena, E.S., Silberberg, S.D., Steckler, T., and Wurbel, H. (2020). The ARRIVE guidelines 2.0: Updated guidelines for reporting animal research. PLoS Biol. *18*, e3000410. https://doi.org/10.1371/journal.pbio.3000410.
79. Kulak, N.A., Geyer, P.E., and Mann, M. (2017). Loss-less Nano-fractionator for High Sensitivity, High Coverage Proteomics. Mol. Cell. Proteomics *16*, 694–705. https://doi.org/10.1074/mcp.O116.065136.
80. Meier, F., Brunner, A.-D., Frank, M., Ha, A., Bludau, I., Voytik, E., Kaspar-Schoenefeld, S., Lubeck, M., Raether, O., Bache, N., Aebersold, R., Collins, B.C., Rost, H.L., and Mann, M. (2020). diaPASEF: parallel accumulation-serial fragmentation combined with data-independent acquisition. Nat. Methods *17*, 1229–1236. https://doi.org/10.1038/s41592-020-00998-0.
81. Schindelin, J., Arganda-Carreras, I., Frise, E., Kaynig, V., Longair, M., Pietzsch, T., Preibisch, S., Rueden, C., Saalfeld, S., Schmid, B., Tinevez, J.Y., White, D.J., Hartenstein, V., Eliceiri, K., Tomancak, P., and Cardona, A. (2012). Fiji: an open-source platform for biological-image analysis. Nat. Methods *9*, 676–682. https://doi.org/10.1038/nmeth.2019.
82. Silversmith, W. (2021). cc3d: Connected components on multilabel 3D & 2D images. https://doi.org/10.5281/ZENODO.5535250.
83. Cox, J., Hein, M.Y., Luber, C.A., Paron, I., Nagaraj, N., and Mann, M. (2014). Accurate Proteome-wide Label-free Quantification by Delayed Normalization and Maximal Peptide Ratio Extraction, Termed MaxLFQ. Mol. Cell. Proteomics *13*, 2513–2526. https://doi.org/10.1074/mcp.M113.031591.
84. Bruderer, R., Bernhardt, O.M., Gandhi, T., Miladinović, S.M., Cheng, L.-Y., Messner, S., Ehrenberger, T., Zanotelli, V., Butscheid, Y., Escher, C., Vitek, O., Rinner, O., and Reiter, L. (2015). Extending the Limits of Quantitative Proteome Profiling with Data-Independent Acquisition and Application to Acetaminophen-Treated Three-Dimensional Liver Microtissues. Mol. Cell. Proteomics *14*, 1400–1410. https://doi.org/10.1074/mcp.M114.044305.
85. Callister, S.J., Barry, R.C., Adkins, J.N., Johnson, E.T., Qian, W.j., Webb-Robertson, B.-J.M., Smith, R.D., and Lipton, M.S. (2006). Normalization Approaches for Removing Systematic Biases Associated with Mass Spectrometry and Label-Free Proteomics. J. Proteome Res. *5*, 277–286. https://doi.org/10.1021/pr050300l.
86. Demichev, V., Messner, C.B., Vernardis, S.I., Lilley, K.S., and Ralser, M. (2020). DIA-NN: neural networks and interference correction enable deep proteome coverage in high throughput. Nat. Methods *17*, 41–44. https://doi.org/10.1038/s41592-019-0638-x.
87. Tyanova, S., Temu, T., Sinitcyn, P., Carlson, A., Hein, M.Y., Geiger, T., Mann, M., and Cox, J. (2016). The Perseus computational platform for comprehensive analysis of (prote)omics data. Nat. Methods *13*, 731–740. https://doi.org/10.1038/nmeth.3901.
88. Wiśniewski, J.R., Hein, M.Y., Cox, J., and Mann, M. (2014). A "Proteomic Ruler" for Protein Copy Number and Concentration Estimation without Spike-in Standards. Mol. Cell. Proteomics *13*, 3497–3506. https://doi.org/10.1074/mcp.M113.037309.

STAR★METHODS

KEY RESOURCES TABLE

REAGENT or RESOURCE	SOURCE	IDENTIFIER
Antibodies		
Iba1	Wako	Cat.# 019–19741; RRID: AB_839504
Stathmin 1	Novus Biologicals	Cat.# NBP1-76798; RRID:AB_11015725
Neurocan	abcam	Cat.# ab31979; RRID:AB_2149711
S100a11	R&D	Cat.# MAB5167; RRID:AB_1207907
Thop1	Novus Biologicals	Cat.# NB400-146; RRID:AB_10128241
MOAB2	Novus Biologicals	Cat.# NBP2-13075; RRID:AB_2923428
Goat anti-rabbit IgG Alexa Fluor 647	Invitrogen	Cat.# A21245; RRID:AB_2535813
Goat anti-Mouse IgG Alexa Fluor 488	Invitrogen	Cat.# A11029; RRID:AB_2534088
Goat anti-Mouse IgG Alexa Fluor 594	Invitrogen	Cat.# A11032; RRID:AB_2534091
Goat anti-Rat IgG Alexa Fluor 594	Invitrogen	Cat.# A11007; RRID:AB_10561522
Goat anti-Rat IgG Alexa Fluor 488	Invitrogen	Cat.# A11006; RRID:AB_141373
Atto647N conjugated anti GFP nanobooster	Chromotek	Cat.# gba647n-100; RRID:AB_2629215
Chemicals, peptides, and recombinant proteins		
Congo Red	Sigma-Aldrich	Cat.#C6277
Propidium iodide (PI)	Sigma-Aldrich	Cat.#P4864
Paraformaldehyde (PFA)	Sigma-Aldrich	Cat.#P6148
Tetrahydrofuran (THF)	Sigma-Aldrich	Cat.# 186562
tert-butanol	Sigma-Aldrich	Cat.# 360538
Dichloromethane (DCM)	Sigma-Aldrich	Cat.# 270997
Diphenyl ether (DPE)	Alfa Aesar	Cat.# A15791
Vitamin E (DL-alpha-tocopherol)	Alfa Aesar	Cat.# A17039
Benzyl benzoate	Sigma-Aldrich	Cat.#W213802
Benzyl alcohol	Sigma-Aldrich	Cat.# 24122
CHAPS	Carl Roth	Cat.# 1479.4
N-Methyldiethanolamine	Sigma-Aldrich	Cat.# 471828
Trypsin	Sigma-Aldrich	Cat.#T6567
Formic acid	Sigma-Aldrich	Cat.# 64-18-6
Acetonitrile	Sigma-Aldrich	Cat.# 75-05-8
Experimental models: Organisms/strains		
$CX_3CR\text{-}1^{GFP}$ mice: B6.129P2(Cg)-$Cx3cr1^{tm1Litt}$/J	Jackson Laboratory	Strain # 005582; RRID: IMSR_JAX:005,582
Thy1-GFP-M mice: Tg(Thy1-EGFP)MJrs/J	Jackson Laboratory	Strain # 007788; RRID: IMSR_JAX:007,788
5xFAD: B6.Cg-Tg(APPSwFlLon, PSEN1*M146L*L286V)6799Vas/Mmjax	Jackson Laboratory	Strain #034848-JAX; RRID: MMRRC_034848-JAX
LysM-eGFP: B6.129(Cg)-*Lyz2*$^{tm1.1Graf}$/Mmmh	MMRC	Strain #012039-MU; RRID: MMRRC_012039-MU
C57BL/6J mouse line	Jackson Laboratory	Strain #:000,664; RRID: IMSR_JAX:000,664
Software and algorithms		
ImSpector	Aberrior/LaVision	https://www.lavisionbiotec.com
Imaris	Bitplane AG	https://imaris.oxinst.com/
Vision4D	Arivis	https://www.arivis.com/de/imaging-science/arivis-vision4d
Fiji	Schindelin et al.[81]	https://ImageJ.net/software/fiji/

(*Continued on next page*)

Continued		
REAGENT or RESOURCE	SOURCE	IDENTIFIER
syGlass VR	syGlass	https://www.syglass.io
Ansys Academic Research Mechanical	Ansys	https://www.ansys.com/academic
RoboDK 5.5	RoboDK Software S.L.	https://robodk.com/
MaxQuant (1.6.7.0)	Tyanova et al.[87]	https://maxquant.org/
Perseus (1.6.7.0)	Tyanova et al.[87]	https://maxquant.org/perseus/
GraphPad Prism(8.2.1)	GraphPad Software	https://www.graphpad.com
Code for 2D to 3D image registration	This Paper	Methods S1
Deposited Data		
Mass spectrometry raw data, libraries and outputs	This paper	https://www.ebi.ac.uk/pride/; ID# PXD034027 and PXD025316
Others		
18G A-max paed Bone marrow biopsy needle 40,901,803	HVM Medical Products GmbH	https://hvm-medical.com/produktkatalog-biopsie/
22G Chiba Fine Needle 07,742,208	HVM Medical Products GmbH	https://hvm-medical.com/produktkatalog-biopsie/

RESOURCE AVAILABILITY

Lead contact

Further information and requests for resources should be directed to and will be fulfilled by the Lead Contact, Ali Ertürk (erturk@helmholtz-muenchen.de).

Materials availability

This study did not generate new unique reagents.

Data and code availability

- All mass spectrometry raw data, libraries and outputs from each particular search engine analyzed in this study have been deposited to the ProteomeXchange Consortium via the PRIDE partner repository with the dataset identifier: Database: PXD034027 and Database: PXD025316.
- The source code for registration of 2D to 3D images is provided in supplemental information under Methods S1.
- Any additional information required to reanalyze the data reported in this work paper is available from the Lead Contact upon request.

EXPERIMENTAL MODEL AND SUBJECT DETAILS

Animals

We used the following animals in the study: mixed gender for CX3CR1-eGFP (10 months old), males only for Thy-1-GFPM (10 months old), mixed gender for 5xFAD (6 weeks and 6-months old), mixed gender for LysM-eGFP (3 months old) and mixed gender for C57Bl6/J (3 months old) from Jackson Laboratory. The animals were housed under a 12/12 h light/dark cycle. The animal experiments were conducted according to institutional guidelines: Klinikum der Universität München/Ludwig Maximilian University of Munich and after approval of the Ethical Review Board of the Government of Upper Bavaria (Regierung von Oberbayern, Munich, Germany) and the Animal Experiments Council under the Danish Ministry of Environment and Food (2015-15-0201-00535) and following the European directive 2010/63/EU for animal research. All data are reported according to the ARRIVE.[78] Sample sizes were chosen based on prior experience with similar models.

Human samples

Intact human brains from a 92 years-old female and intact heart from a 97 years-old female were taken from human body donors with no known neuropathological diseases. The donors gave their informed and written consent to explore their cadavers for research and educational purposes, when still alive and well. The signed consents are kept at the Anatomy Institute, University of Leipzig, Germany. Institutional approval was obtained in accordance to the Saxonian Death and Funeral Act of 1994. The signed body donor consents are available on request.

METHOD DETAILS

Repeated closed head mild traumatic brain injury (mTBI)

Before mTBI, tin foil was taped and tightened to the U-shaped stage made of clear plastic container (38 × 27 × 27 cm^3) containing a sponge collection (38 × 25 × 15 cm^3). Then, mice were pre-treated with buprenorphine (1:15 saline, 50ul/20mg, ip) and anesthetized with 4% isoflurane using 1.0 L min^{-1} air until non-responsive to a paw or tail pinch. To ensure the head acceleration and rotation following the head impact, the mice were placed under an impact tip on the tin foil, which contains holes according to the shape of a mouse and can support the body weight of the mice. The mice were kept under light anesthesia with continued 2% isoflurane. mTBI was produced using a stereotaxic impactor device with a 5-mm round tip coated with 1mm thick rubber, which can preserve an intact skull after impact. The impact tip was placed and covered the scalp's area from just behind the eyes to the midline of the ears, the center of the tip at approximately midway along the sagittal suture. The injury was produced without skin incision (velocity of 5 m/s, depth of 0.5mm, and dwell time of 0.1 s). The mouse was removed quickly from the collection sponge and transferred to the recovery box maintained at 32 °c. In total, mice received four hits with a 48 h interval in seven days. Sham mice receive identical handling and exposure to the same time length of anesthesia as the mTBI mice but receive no impact.

Perfusion and tissue preparation

Mice were anesthetized using a combination of midazolam, medetomidine and fentanyl (MMF) (1mL/100g of body mass for mice; i.p.). As soon as the animals did not show any pedal reflex, they were intracardially perfused with cold heparinized 0.1 M PBS (10 U/mL of Heparin, Ratiopharm; 100–125 mmHg pressure using a Leica Perfusion One system) for 5–10 min at room temperature until the blood was washed out, followed by ice-cold 4% paraformaldehyde (PFA) in 0.1 M PBS (pH 7.4) (Sigma) for 10 min. Then, the brains were extracted and post-fixed in 4% PFA for 1 day at 4°C and later washed with 0.1 M PBS for 10 min 3 times at room temperature. The whole brain clearing or nanoboosting procedure was started immediately. For the collection of fresh frozen samples, animals were sacrificed by cervical dislocation and brains were quickly snapped frozen in liquid nitrogen and stored in −80°C until further processing.

Congo red labeling of whole brains of 5xFAD animals

Whole brains were dehydrated with gradual addition of methanol in PBS (50% x1, 80% x1, 100% x2, each for 1 h). Overnight bleaching with 5% hydrogen peroxide in methanol was done at 4°C. Brains were then gradually rehydrated in 100%, 80%, 50% methanol in PBS (1 h for each step, followed by 2 additional washes in PBS). Detergent washing was then performed in PBS with 0.2% Triton X-100 for 2 h, brains were incubated overnight at 37°C in PBS with 0.2% Triton X-100 and 0.3 M glycine, followed by blocking in PBS with 0.2% Triton X-100 and 6% goat serum for 7 days. Following blocking, the tissue was washed for 1 h twice in PBS with 0.2% Tween 20 and 10 μg/mL heparin (PTwH). Next, brains were incubated with 10 μM Congo Red (Sigma, C6277) at 37°C in PTwH for 5 days. After that, brains were washed in PTwH for 2 days with periodic solution changes and gradually dehydrated using 3DISCO clearing as described next.

Clearing of brains using DISCO methods

We followed the 3DISCO and uDISCO passive clearing protocol as described previously. In brief, dissected brains were placed in 5 mL tubes (Eppendorf, 0,030,119.401) and covered with 4.5 mL of clearing solution. All incubation steps were performed in a fume hood with gentle shaking or rotation, with the samples covered with aluminum foil to keep them in dark. To clear the samples using 3DISCO, gradient of tetrahydrofuran (THF) in distilled water (v/v %), 2 h for each step, was used as 50%, 70%, 90%, 100% and overnight 100% THF; after dehydration, the samples were incubated for 45 min in dichloromethane (DCM, Sigma, 270,997), and finally in BABB (benzyl alcohol + benzyl benzoate 1:2, Sigma, 24,122 and W213802) until transparency. Next for uDISCO a gradient of tert-butanol (Sigma, 360,538) in distilled water (v/v %) was used as 50, 70, 90, 100 twice at 32°C for 12 h each step, followed by immersion in DCM for 45 min at room temperature and finally incubated with the refractive index matching solution BABB-D15 containing 15 parts BABB, 1 part diphenyl ether (DPE) (Alfa Aesar, A15791) and 0.4% Vol vitamin E (DL-alpha-tocopherol, Alfa Aesar, A17039), for at least 6 h at room temperature until achieving transparency.

vDISCO whole-brain passive immunostaining, clearing and imaging

Passive vDISCO was performed on dissected organs as performed by Cai R et al. First, the post-fixed brains were pre-treated with permeabilization solution containing 1.5% goat serum, 0.5% Triton X-100, 0.5 mM of Methyl-beta-cyclodextrin, 0.2% *trans*-1-Acetyl-4-hydroxy-L-proline and 0.05% Sodium Azide 0.1 M for 2 days at 37°C with gentle shaking. Subsequently, the brains were incubated in 4.5 mL of this same permeabilization solution plus the nanobooster Atto647N conjugated anti-GFP (1:600, which is ∼5–8 μg of nanobooster in 4.5 mL) for CX3CR1-eGFP and Thy-1-GFPM brains for 12–14 days at 37°C with gentle shaking, then brains were washed for 2 h 3 times and once overnight with the washing solution (1.5% goat serum, 0.5% Triton X-100, 0.05% of sodium azide in 0.1 M PBS) at room temperature and in the end washed for 2 h 4 times with 0.1 M PBS at room temperature. The immunostained brains were cleared with 3DISCO clearing first they were put in the Eppendorf 5 mL tubes and then incubated at room temperature with gentle shaking in 4.5 mL of the following gradient of THF in distilled water (v/v %), 2 h for each step: 50, 70, 90, 100 THF and

overnight 100% THF; after dehydration, the samples were incubated for 45 min in DCM, and finally in BABB until transparency. During all the clearing steps, the tubes were wrapped with aluminum foil to keep them in dark.

vDISCO whole body immuno labeling, clearing and imaging

The detailed protocol of vDISCO was described previously.[34] The mouse bodies were placed inside a 300 mL glass chamber (Omnilab, 5,163,279), to be filled with the appropriate solution regarding the protocol to cover the entire body of the animal (~250–300mL). A transcardial circulator system was established in order to allow peristaltic pumping of the solutions (ISMATEC, REGLO Digital MS-4/8 ISM 834; reference tubing, SC0266), with the pressure being set at 180–230 mmHg (50–60 rpm). The tubing was set to allow pumping of the solutions through the heart (attached to a perfusion needle (Leica, 39,471,024)) into the vasculature with the same entry point used for PBS and PFA perfusion steps described above. The other end of the tube was immersed into the chamber with a loose end to allow suction of the solution into the body. The samples were initially perfused with a decolorization solution (25% of CUBIC reagent 1 (55) which is composed of 25 wt % urea (Carl Roth, 3941.3), 25 wt % N,N,N′,N′-tetrakis (2-hydroxypropyl) ethylenediamine (Sigma, 122,262) and 15 wt % Triton X-100 (AppliChem, A4975,1000) in 0.1 M PBS)) for 2 days, refreshing the solutions every 12h. Samples were washed with PBS for 3 × 2h. Then, decalcification solution (10 w/v % EDTA in 0.01 PBS, pH~8–9, Carl Roth, 1,702,922,685) was perfused for 2 days followed by half a day with permeabilization solution composed of 0.5% Triton X-100, 1.5% goat serum (GIBCO, 16,210,072), 0.5 mM of Methyl-beta-cyclodextrin (Sigma, 332,615), 0.2% *trans*-1-Acetyl-4-hydroxy-L-proline (Sigma, 441,562), 0.05% sodium azide (Sigma, 71,290) in 0.01 M PBS. The setup was adjusted to initiate the PI labeling and boosting. The free end of the perfusion tube was connected to a 0.22 μm syringe filter (Sartorius, 16,532) and an infrared lamp (Beuer, IL21) was aimed at the chamber to enable the solution's temperature to be around 26–28°C. This setup was then left running for 6 days after the addition of 35 μL of nanobooster (stock concentration 0.5–1 mg/mL) and 290 μL of propidium iodide (stock concentration 1 mg/mL) which was added directly into the refreshed permeabilization solution. Next, the body was placed into a 50 mL tube (Falcon, 352,070), with the same permeabilization and labeling solution, and an extra 5 μL of nanobooster was added. The tube was then put on a shaker at RT for 2 additional days for labeling. Atto647N conjugated anti GFP nanobooster (Chromotek, gba647n-100) and propidium iodide (PI, Sigma, P4864) was used to boost the signal from the LysM-eGFP animals and stain cell nuclei respectively in the study. Then, the animals were placed back into the initial perfusion setup, where washing solution was perfused for 2 × 12h, which was composed of; 1.5% goat serum, 0.5% Triton X-100, 0.05% of sodium azide in 0.1 M PBS. 0.1 M PBS was used to wash the sample 3 × 2h. 3DISCO protocol was applied for whole body clearing. The animals were demounted from the perfusion system but kept in glass chambers and placed on top of shakers (IKA, 2D digital) at room temperature inside a fume hood. Glass chambers were sealed with parafilm and covered with aluminum foil along with the 3DISCO application. For dehydration, sequential immersion of tetrahydrofuran (THF) (Sigma,186,562) (50 vol % THF, 70 vol % THF, 80 vol % THF, 100 vol % THF and again 100 vol % THF) was applied every 12 h. Then 3 h of dichloromethane (DCM) (Sigma, 270,997) immersion for delipidation was followed by indefinite immersion in BABB (benzyl alcohol + benzyl benzoate 1:2, Sigma, 24,122 and W213802) solution for refractive index matching.

SHANEL sample preparation and clearing

Archived human samples were obtained in PFA which were stored for a long period of time (>5 years) at 4°C and subjected to our previously published SHANEL clearing protocol with some modifications.[4] Briefly, samples were dehydrated with EtOH/dH_2O series at RT: 50%, 70%, 100% for 1 h for each step, then incubated with 10 mL DCM/MetOH (2:1 v/v) (freshly prepared) for 6h at RT followed by rehydration with EtOH/dH_2O series at RT: 100%, 70%, 50%, dH_2O for 1 h each step then incubated with 0.5M acetic acid (30 mL/L) at RT for 2 h, then wash with dH_2O twice for 15 min and then incubated with 4M guanidine hydrochloride (382.12 g/L), 0.05M sodium acetate (4.1 g/L), 2% v/v Triton X-100 in dH_2O, (measure pH: 6.0) at RT for 2 h, then wash with dH_2O twice for 15 min each and wash with PBS twice for 15 min each. Afterward samples were incubated with 10% CHAPS, 25% N-Methyl diethanolamine in dH_2O at 37°C for 4 h and then washed with dH_2O twice for 15 min each. Since we did not perform any deep antibody labeling in these samples, we started clearing these samples without prior blocking or antibody labeling steps. Clearing was done with THF in water with dilutions (v/v %) of 50%, 70%, 90%, 100%, 1h each, 100% overnight, DCM 45 min and incubated in BABB until the samples were transparent.

Behavioral assessment

Barnes maze

Briefly, a maze consisting of a surface bright circular platform with an escape black box can be recessed and located at the bottom of one of the 20 holes. Visual shapes were placed on 3 walls of the room as cues. For all trials, mice were placed in a cylinder black start chamber in the center of the maze for 10 s. After the chamber lifted and the test started, mice were given 3 min to locate and enter the target box during the spatial acquisition time. For a period of 4 days, 4 trials were given per day with an inter-trial of 15 min. The trial ended when the mouse entered the escape box or after 3 min had elapsed. Mice were allowed to remain in the escape box for 1 min. A system (Ethovision XT) was used to continually track and record the movement of the mice. Escape latency was measured as the time taken for the mouse to enter the box.

Assessment of motor function

The mice were given 3 trials training per day for 3 days to walk along a 1 cm diameter and 100 cm long wood beam with a goal box on the end of the beam before mild TBI. The beam was placed 1 m above ground. The latency that it takes walking to cross the beam after 8 weeks from mild TBI were recorded. Mice that were unable to cross the beam were removed in the training.

Immunofluorescence and confocal microscopy

Briefly, mice were sacrificed after 8 weeks of injury or at six weeks of age following transcardial perfusion with PBS and with 4% cold PFA. Brains were post-fixed in 4% PFA at 4°C overnight. Either frozen sections or cleared-rehydrated frozen sections were treated with 0.2% Triton X-100 in PBS for 15 min, blocked for 1 h at room temperature with 10% serum in PBST. Then incubation with primary antibodies Iba1 (1:1000, Wako, 019–19741), Stathmin 1 (1:300, Novus, NBP1-76798), Neurocan (1:300, abcam, ab31979), S100a11 (1:300, R&D, MAB5167), Thop1 (1:300, Novus, NB400-146), MOAB2 (1:1000, Novus, NBP2-13075), at 4°C for overnight and Alexa conjugated secondary antibodies (1:1000, Goat anti-rabbit IgG Alexa Fluor 647, Invitrogen, A21245; Goat anti-Mouse IgG Alexa Fluor 488, A11029; Goat anti-Mouse IgG Alexa Fluor 594, A11032; Goat anti-Rat IgG Alexa Fluor 594, A11007; Goat anti-Rat IgG Alexa Fluor 488, A11006) were incubated for 1 h at room temperature. Slices were mounted after being stained with Hoechst 33,342 (Invitrogen). Images were acquired with 10x, 40x, and 63× objective of confocal microscope (ZEISS LSM880).

Light-sheet microscopy and image processing

Single plane illuminated (light-sheet) image stacks were acquired using an Ultramicroscope II (LaVision BioTec) and UltraMicroscope Blaze (Miltenyi Biotec), featuring an axial resolution of 4 μm with following filter sets: ex 470/40 nm, em 535/50 nm; ex 545/25 nm, em 605/70 nm; ex 640/40 nm, em 690/50 nm. Whole brains were imaged individually using high magnification objectives: 4× objective (Olympus XLFLUOR 4× corrected/0.28 NA [WD = 10 mm]), LaVision BioTec MI PLAN 12× objective (0.53 NA [WD 10 = mm]) coupled to an Olympus revolving zoom body unit (U-TVCAC) kept at 1x. High magnification tile scans were acquired using 20-35% overlap and the light-sheet width was reduced to obtain maximum illumination in the field. Processing, data analysis, 3D rendering and video generation for the rest of the data were done on an HP workstation Z840, with 8 core Xeon processor, 196 GB RAM, and Nvidia Quadro k5000 graphics card and HP workstation Z840 dual Xeon 256 GB DDR4 RAM, nVidia Quadro M5000 8GB graphic card. We used Imaris (Bitplane), Fiji (ImageJ2), Vision 4D (Arivis) and syGlass (for 3D and 2D image visualization). Tile scans were stitched by Fiji's stitching plugin49.

Registration of light-sheet and LCM images to correlate probe selection

In order to map the proteomic samples to the whole brain light-sheet imaging we developed a registration protocol. The LCM method is acquired in order to select the ROI to be cut from the sample of brain tissue. The registration of light-sheet and LCM images is very challenging because it is a multimodal registration problem and the imaged tissue undergoes physical changes when the re-clearing process is applied after the light-sheet imaging, introducing scale differences and sometimes even damaged tissue. Moreover, the tissue contrast and lighting distribution are different.

For the purpose of registering the images, we acquired consecutive 2D LCM slices (0.65 x 0.65 μm^2, slice thickness 12 um) which correspond to the 3D light-sheet volume (1.63 × 1.63 × 4 μm^3). We down sampled all images to the largest dimension to achieve an isotropic resolution of 12um. We experimented with a multitude of registration steps, such as: 3D-3D volume registration, 2D-2D slice registration, various transformations (rigid, affine, BSpline), edge extraction, binary thresholding, normalization strategies, and similarity metrics. We found the best performance for the following protocol using elastix:

1) Pre-processing: Both LCM and light-sheet images were clipped to the relevant contrast ranges and normalized to the [0, 255] range. Additionally, the LCM slices undergo histogram equalization to mitigate the severe lighting differences, 2) first, a single LCM slice is rigidly registered to each 3D light-sheet slice 3) next, we calculate different image similarity scores between the registered LCM slice and its corresponding LS slice. We choose the most similar slices as an initial match in z-Dimension 4) then, we create a 3D LCM volume by padding the single LCM slice and then do a full 3D affine registration to the 3D light-sheet volume to account for scaling differences. These four steps lead to our registration result, where the two red boxes indicate a potential cut region of interest in the LCM image and its corresponding spatial location in the light-sheet image. We find that the registration of the individual LCM slices is very successful, whereby the equalization plays a crucial role. The rigid registration is also able to find a good initialization for the affine registration in the next step. The third step poses harder challenges, as the differences between the LCM and light-sheet images outlined above persist. For example, we observe that the brightness of the light-sheet image increases radially outwards, whereas in the LCM the light is more region-dependent. Furthermore, in the LCM images various regions are so hypointense, that even the extraction of low-level features such as edges is not very informative for the registration. These challenges particularly impact the registration of the LCM volume in the z direction. We are convinced that this registration problem is a highly non-trivial task and believe that future research will be of high relevance for the community beyond our application.

Optimization of cleared tissue for cryopreservation and sectioning

After acquiring the whole brain images from CX3CR1-eGFP, 5xFAD, C57BL/6J mice the brains were further optimized for cryopreservation and sectioning. The course of tissue clearing and imaging in BABB makes the tissue brittle and hard to process further. To solve this, we rehydrated the samples with the respective clearing solutions to be able to process samples for cryosectioning.

Thereafter, samples were washed with PBS twice for 15 min each and cryopreserved overnight with 30% sucrose solution in 4°C. To avoid any ice crystals formation, samples were further embedded in Optimal cutting temperature compound (OCT compound) under the chilled isopentane container placed on dry ice. Samples were stored in −80°C until cryosectioning.

Laser-capture microdissection

For the microdissection of cells and plaques, we used both the PALM Micro-Beam system (Zeiss) and Leica LMD 7000 (Leica). PALM Micro-Beam uses a focused laser beam to cut out and isolate the selected specimen without contact. The laser catapult quickly isolates the region of interest and uncontaminated in the adhesive cap mounted in the RoboMover upwards. The Leica system projects the samples downwards. Briefly, in case of the PALM system, after cryosectioning, sections were mounted on the polyethylene naphthalate (PEN, Zeiss) slides and were either stored at −80°C in 50 mL falcon tubes filled with molecular sieves (Sigma-Aldrich) or processed further for serial dehydration with ethanol and air dried for 15 min under the hood. Cells in the optic tract from mTBI/Sham brains and amyloid-beta plaques from the 5xFAD and from respective WT brain regions were micro-dissected by laser pressure catapulting (LPC) UV LCM system (Palm Zeiss Microlaser Technologies, Munich, Germany) consisting of an inverted microscope with a motorized stage, an UV laser and an X-Cite 120 fluorescence illuminator (EXFO). The microdissection process was visualized with an AxioCam ICc camera coupled to a computer and was controlled by Palm RoboSoftware (Zeiss, Germany). An area of approximately 200 × 200 μm (corresponding to 40–60 cells) were cut by laser using a 20× objective (LD Plan-Neofluar 20×/0.4 corr M27) and catapulted against gravity into the adhesive cap. Tissues were quickly lysed in 20 μL of lysis buffer, spun down and kept in dry ice or stored in −80°C. To avoid any uncertainties in capturing ROI, each time after catapulting as well as after lysing and spun down, the cap was examined under the camera.

Automated robotic proteomic probe extraction from whole body

The strategy applied in this study was image guided extraction of targeted samples in the bone marrow of scapula and cranium on whole mouse body with a precise robotic biopsy solution. The imaging takes place under the Ultramicroscope Blaze manufactured by Miltenyi Biotec. The robotic arm Meca500 R3 manufactured by Mecademic Robotics is used to control the motion of the needle sets to extract multiple targets. During the imaging, the embedded whole mouse body was placed on a bed designed for this study that holds the sample stable under the load applied by the needle. The Meca500 was mounted above the microscope to utilize the slim gap between the submerged lens and the walls of the sample bath for the operation on the mouse during live imaging. The extraction was conducted by using two sizes of biopsy needles with stylets sealing the shaft of the needle to prevent unwanted tissue contamination while approaching the target. The larger diameter needle was fixed on the robotic arm with a holder designed and manufactured to ensure the access of the finer needle to the target with precision.

Precision and accuracy of sampling

The most important problem to overcome in the deep tissue sampling in a whole mouse body is to achieve the required precision and accuracy of the sampling needle tip. Since the operation happens in toughened, inhomogeneous multilayer tissue, the forces acting on the needle and the tissue during the penetration are highly fluctuating and axially asymmetric. The borders of two different types of tissues e.g., bone and muscle, tend to deflect the needle in the direction of the muscle. These forces result in bending of the needle which leads to inaccuracies when approaching the target. Since it is problematic to move the needle sideways or rotate it inside the tissue due to high traction, it is complicated to compensate for the inaccuracy after the needle has penetrated into the tissue.

Providing precision and accuracy to the operation requires every component on the load path to remain as rigid as possible. The translational stage of the microscope is fixed on the main structure and holds the mouse bed, the mouse bed supports the agarose embedding around the mouse and the agarose embedding supports the whole mouse body including the extremities and inner organs. On the other end of the setup the robotic arm was fixed on the main structure. The needle holder is screwed on the last actuator of the robot arm. The needle is fixed on the needle holder with a screw. The load transfer mechanism can be reduced to some basic components to model the bending behavior of the structure and calculate the deflections. The total deflection of all these components under load is optimized to provide an accurate positioning of the needle deep in the tissue.

Needle gauge

The needle gauge plays a key role in the total deflection. The needle can be considered as a cylindrical cantilever beam and the maximum deflection on the needle caused by a concentrated load at the tip is defined by the formula:

$$\delta_{max} = \frac{Pl^3}{3EI}$$

In this equation the maximum deflection δ_{max} is proportional to the force applied on the tip P, proportional to the cube of the length of the needle l and inversely proportional to the Young's modulus of the needle's material E and the static moment of inertia I.

The needle's deflection in the deep tissue is not only caused by the concentrated force applied on the piercing tip, but also by the distributed load on the needle, for which case the deflection at the tip is defined by the formula: $\delta_{max} = \frac{\omega l^4}{8EI}$.

In this case the maximum deflection δ_{max} is proportional to the distributed load applied on the needle ω, proportional to the 4th power of the length of the needle *l* and inversely proportional to the Young's modulus of the needle's material *E* and the static moment of inertia *I*. The static moment of inertia *I* can be calculated as:

$$I_y = I_z = \frac{\pi\left(R^4 - r^4\right)}{4}$$

For both of these equations the static moment of inertia *I* is proportional to the difference of the 4th power of the outer *R* and inner *r* radii of the needles. These calculations suggest a 22G needle would deflect around 9 times further away from target in comparison to an 18G needle.

Although a larger needle is more accurate meeting the target due to lower deflection, there are also disadvantages such as collecting a larger sample including unwanted neighboring tissue. Furthermore, since the penetration area is larger with a larger needle, the force required to achieve the penetration stress on the tissue is also larger. Occasionally, it becomes impossible to apply the necessary force for penetration, since the tissue cannot support such loads and the harder bone tissue gets pushed into the softer muscle tissue. We found that the optimum solution to this problem was using two needles in combination. The procedure applied in this study was to extract bone marrow with 18G blunt tip biopsy needle A-MAX PAED and 22G Chiba biopsy needle. Both of these needles include a stylet to block the hollow shaft of the needle until the biopsy target is reached. Initially the 18G needle was fixed on the needle holder on the Meca500 and the coordinates of the tip of the needle are calibrated under the microscope. The needle is advanced with the Meca500 axially to the coordinates where the stylet is about to touch the target. Then the 18G stylet is removed to create an open channel for the 22G needle to move until the target without any resistance or deflection. As soon as the 22G needle reaches the target the 22G stylet is removed from the needle and the target is sucked in to the needle's shaft with the slight vacuum supplied by a syringe and the chopping motion of the beveled needle tip around the target. When the targets acquisition is confirmed observing the light sheet image, the needle is retracted without stopping or increasing the vacuum applied by the syringe and the sample is deployed into a low binding 0.5 mL Eppendorf tube with some extra ECi (ethyl-cinnamate) to make sure any remaining pieces of the sample in the needle is flushed before the next target.

Specimen holder and needle holder strategy

During the imaging process the sample and the lens are submerged into an imaging solution with a refractive index of 1.56. The common options for this medium are mostly ECi or benzyl benzoate and benzyl alcohol (BABB) solution with a 2:1 ratio. The mouse holder and needle holder are manufactured using the clear resin on a Form3 manufactured by Formlabs. This process provides agile prototype iterations but the manufactured parts lose their integrity and start falling apart upon contact with BABB. Therefore, these experiments are conducted under ECi. The mouse bed and the needle holder are modeled using finite elements method (FEM) to simulate their behavior under loading using Ansys Academic Research Mechanical 2022 R2. Using the stresses and deflections calculated from the static FEM analyses, an iterative method was employed to optimize the structures of the mouse bed and the needle holder. The mass of the mouse bed was reduced to around 80 g and the needle tip to around 20 g, while the simulated total deflection of both pieces combined was reduced to less than a millimeter from an initial total deflection around 7mm under extreme load conditions such as 40 N axial load applied on the needle and the same amplitude applied on the mouse bed in the direction of needle's approach.

Embedding of the whole mouse body

Although the whole mouse body is cleared and fixed, it still deflects far enough for the needle to miss the target. Especially when the target is in a bone, the forces required for penetration go beyond 10N with the 18G needle. Embedding the body with a gel or resin is crucial to limit the deformation of the mouse body. The uneven structure of the internal organs, gaps in the chest cavity and curved outer surfaces create incalculable sources for tissue and needle deflection. To stabilize the cleared mouse bodies during robotic tissue extraction, they had to be embedded in a block of agarose. To do this, we prepared a 2% (w/v) solution of agarose by dissolving the agarose powder in deionized water. This mixture was heated in a microwave until the agarose had completely dissolved. Then, the mixture was allowed to cool until it had reached a temperature of about 50–60°C. This cooled agarose solution was then poured onto the sample, and it was left to cool until it had completely solidified. After it had solidified, excess parts of agarose around the samples were carefully trimmed away using a sharp scalpel.

To clear the agarose and prepare it for light sheet imaging, the sample was dehydrated in a serial dilution of tetrahydrofuran (ROTISOLV, Carl Roth). The dilutions used were as follows: (v/v) 20%, 30%, 50%, 70%, 90%, 100% -2x. After the sample had completely dehydrated, it was immersed in a solution of BABB which is a mixture of benzyl alcohol and benzyl benzoate to complete the clearing process. The sample was immersed in these solutions for a minimum of 24 h at every stage.

Manipulation system

A common solution for micrometer accurate targeting is a micromanipulator but in this study the target was located deep in the hardened and tough tissue. Considering the force required in case of a bone penetration is in the range of 10 N and micromanipulators operate in the range of hundreds of mN, the standard solution would not suffice for this specific problem.

For the image guided sample extraction, a robot arm with harmonic drives was selected. The advantages in comparison to a micromanipulator or a piezo electric stage system is the level of applicable force without compromising accuracy. The Meca500 can apply a force of 110N and still remain within a precision tolerance of 5 μm. Being able to control such a force with high precision in a large working envelope with 260mm reach in 6 degrees of freedom, provided us the freedom to conduct experiments with various assembly positions, tool deigns, needle dimensions delivering repeatable results.

The system is controlled via the programming and simulation software for industrial robots RoboDK. The 3D models of the optical table, microscope and other structural parts are assembled corresponding to their real locations in a 3D CAD software and exported as.STEP file to the RoboDK environment. From that point on Meca500 is controlled over TCP/IP socket communication with ASCII commands. Having the whole environment in the control software, paths are calculated in segments to avoid any collision. Any misalignment with the needle tip in real world and computer model is also calibrated in the software before sample extraction.

Optimization of DISCO cleared sample preparation for mass spectrometry analysis

Several conditions and combinations of solubilizing agents for the isolation of proteins from tissue cleared mouse brain, heart, and lung samples were initially evaluated for protein extraction efficiency, peptide recovery, and qualitative and quantitative reproducibility keeping fresh or PFA-fixed as reference. Our goal was to establish a workflow that recovers proteomes that are as similar as possible to non-cleared tissue and is universal for all tissue clearing techniques.

Cleared organs or cryosections were removed from the refractive index matching solution BABB and washed five times with 1x PBS solution. The organ was then flash-frozen and pulverized in a Covaris CP02. Afterward, the samples were resuspended in different protein solubilizing solutions (6% SDS500 mM TrisHCl, pH 8.5 (SDS buffer); 2% Sodium deoxycholate, 100 mM TrisHCl pH 8.5, 10 mM Tris-(2-carboxyethyl)-phosphine (TCEP), 40 mM Chloroacetamide (SDC buffer); 50% Trifluoroethanol, 100 mM TrisHCl, pH 8.5 (TFE buffer), followed by protein extraction at 95°C, 1.000rpm for 45 min. Then the samples were subjected to sonication (Branson) at maximum frequency for 30 cycles at 50% output, followed by another heating step at 95°C, 1.000 rpm for 45 min. From here on, processing steps diverged for each protocol.

Proteins solubilized in the SDS buffer were precipitated with ice-cold acetone at 80% v/v ratio overnight at −80°C, followed by centrifugation at max. g for 15 min at 4°C. The supernatant was removed, the pellet was washed with 5 mL ice-cold 80% v/v Acetone/ddH2O, followed by 30 min precipitation on dry ice. The acetone wash steps were repeated two times for a total of three washes. Proteins solubilized in the TFE buffer, were subjected to solvent evaporation in a SpeedVac at 45°C until dryness before further processing.

In case of SDS-SDC or TFE-SDC protocol, in which SDS or TFE protein extraction was coupled to an SDC-based protein digestion, SDS- or TFE-solubilized proteins were resuspended in 1mL of SDC buffer and heated to 95 °C at 1.000 rpm for 10 min to denature proteins, reduce cysteine bridges and alkylate free cysteine residues. Afterward, samples were sonicated for 15 cycles each 30 s at max power in a Bioruptor, followed by another heating step for 10 min at 95°C, 1.000 rpm in a Thermoshaker.

SDC-only, SDS-SDC, TFE-SDC solubilized protein solutions were cooled down to room temperature, diluted 1:1 with 100 mM TrisHCl, pH 8.5, followed by protein concentration estimation by Nanodrop. Extracted and solubilized proteins were digested overnight at 37°C and 1.000 rpm, with trypsin and LysC at a protein to enzyme w/w ratio of 1:50. Next day, trypsin and LysC were added again at a protein to enzyme w/w ratio of 1:50 and proteins were digested further for 4 h at 37°C, 1.000 rpm. Resulting peptides were acidified with 1% TFA 99% Isopropanol in a 1:1 ratio and vortexed, followed by centrifugation at 22.000 xg RT to pellet residual particles. The supernatant was transferred into a fresh tube and subjected to StageTip clean-up via SDB-RPS. 20 μg of peptides were loaded on two 14-gauge stage-tip plugs. Peptides were washed twice with 200 μL 1% TFA 99% ddH2O followed by 200 μL 1% TFA 99% isopropanol in an in-house-made StageTip centrifuge at 2,000 xg. Peptides were eluted with 100 μL of 5% Ammonia, 80% ACN into PCR tubes and dried at 45°C in a SpeedVac centrifuge (Eppendorf, Concentrator plus). Peptides were resuspended in 0.1% TFA, 2% ACN, 97.9% ddH2O.

After evaluation of protein extraction efficiency, all sample preparation for Fresh, PFA-fixed, uDISCO-, 3DISCO-, SHANEL-cleared tissue was performed following the SDS-SDC protocol. For LCM sample preparation, LCM samples were caught on PCR tubes with adhesive caps and successful isolation was verified by visual inspection. 20μL of SDS-buffer was added to each tube. The tube was closed and vortex for 30 s, followed by centrifugation for 5 min in a table-top centrifuge to 'catch' the LCM sample in the protein solubilization buffer, which was confirmed afterward by visual inspection. Sample preparation was performed as described for the SDS-SDC protocol, except for the following modifications: No shaking during cooking steps; Instead of a Branson sonicator, a Bioruptor was used for each sonication step; No Covaris CP02 was used for crushing the sample; Acetone precipitation was performed at 100 μL total volume; SDC resuspension and protein digestion was performed in a 20 μL volume.

High-pH reversed-phase fractionation

To generate a deep library of experiment-specific precursors, peptides were fractionated at pH 10 with the spider-fractionator.[79] 50 μg of purified peptides were separated on a 30 cm C_{18} column in 96 min and concatenated into 16 or 24 fractions with 2 min exit valve switches. Peptide fractions were dried in a SpeedVac and reconstituted in 2% ACN, 0.1% TFA, 97.9% ddH_2O for LC-MS analysis.

Liquid chromatography and mass spectrometry (LC-MS)

LC-MS was performed on an EASY nanoLC 1200 (Thermo Fisher Scientific) coupled online either to a quadrupole Orbitrap mass spectrometer (Q Exactive HFX, Thermo Fisher Scientific), or a trapped ion mobility spectrometry quadrupole time-of-flight mass spectrometer (timsTOF Pro, Bruker Daltonik GmbH, Germany) via a nano-electrospray ion source (Captive spray, Bruker Daltonik GmbH). Peptides were loaded on a 50 cm in-house packed HPLC-column (75 μm inner diameter packed with 1.9 μm ReproSil-Pur C18-AQ silica beads, Dr. Maisch GmbH, Germany). Sample analytes were either separated using a linear 100min gradient from 5 to 30% B in 80 min followed by an increase to 60% for 4 min, and by a 4 min wash at 95%, a decrease to 5% B for 4 min, and a re-equilibration step at 5% B for 4 min, or separated on a linear 120 min gradient from 5 to 30% B in 90 min followed by an increase to 60% for 10 min, and by a 5 min wash at 95%, a decrease to 5% B for 5 min, and a re-equilibration step at 5% B for 5 min (Buffer A: 0.1% Formic Acid, 99.9% ddH2O; Buffer B: 0.1% Formic Acid, 80% CAN, 19.9% ddH2O). Peptides derived from LCM and matching libraries were separated using a linear 70 min gradient from 3 to 30% B in 45 min followed by an increase to 60% for 5 min, an increase to 95% in 5min, followed by 5 min at 95% B, a decrease to 5% B for 5 min, and an equilibration step at 5% B for 5 min. Flow-rates were constant at 300 nL/min. The column temperature was kept at 60°C by an in-house manufactured oven.

Mass spectrometry analysis for the evaluation of sample preparation on a Q Exactive HFX was performed in data dependent scan mode. For full proteome measurements, MS1 spectra were acquired at 60.000 resolution and an m/z range of 300–1.650 with an automatic gain control (AGC) target of 3E6 ions and a maximum injection time of 20 ms. The top 15 most intense ions with a charge of two to eight from each MS1 scan were isolated with a width of 1.4 Th, followed by higher-energy collisional dissociation (HCD) with a normalized collision energy of 27% and a scan range of 200–2,000 m/z. MS/MS spectra were acquired at 15,000 resolution with an AGC target of 1E5, a minimum AGC target of 2.9E3, and a maximum injection time of 28 ms. Dynamic exclusion of precursors was set to 30 s.

Deep proteomes and comparisons of clearing conditions with the SDS-SDC protocol were acquired on a standard timsTOF Pro in a data-dependent PASEF mode with 1 MS1 survey TIMS-MS and 10 PASEF MS/MS scans per acquisition cycle. Ion accumulation and ramp time in the dual TIMS analyzer was set to 100 ms each and we analyzed the ion mobility range from $1/K_0 = 1.6$ Vs cm^{-2} to 0.6 Vs cm^{-2}. Precursor ions for MS/MS analysis were isolated with a 2 Th window for $m/z < 700$ and 3 Th for $m/z > 700$ in a total m/z range of 100–1.700 by synchronizing quadrupole switching events with the precursor elution profile from the TIMS device. The collision energy was lowered linearly as a function of increasing mobility starting from 59 eV at $1/K_0 = 1.6$ VS cm^{-2} to 20 eV at $1/K_0 = 0.6$ Vs cm^{-2}. Singly charged precursor ions were excluded with a polygon filter (otof control, Bruker Daltonik GmbH). Precursors for MS/MS were picked at an intensity threshold of 2.500 a.u. and re-sequenced until reaching a 'target value' of 20.000 a.u taking into account a dynamic exclusion of 40 s elution.

Peptides derived from LCM samples were acquired on a timsTOF Pro modified for highest ion transmission and sensitivity, as described in Brunner et al., in a data-dependent or data independent acquisition PASEF mode.[10] In DDA, 1 MS1 survey TIMS-MS and 5 PASEF MS/MS scans represents one acquisition cycle. Ion accumulation and ramp time in the dual TIMS analyzer was set to 50 ms each and we analyzed the ion mobility range from $1/K_0 = 1.6$ Vs cm^{-2} to 0.6 Vs cm^{-2}. Precursor ions for MS/MS analysis were isolated with a 2 Th window for $m/z < 700$ and 3 Th for $m/z > 700$ in a total m/z range of 100–1.700 by synchronizing quadrupole switching events with the precursor elution profile from the TIMS device. The collision energy was lowered linearly as a function of increasing mobility starting from 59 eV at $1/K_0 = 1.6$ VS cm^{-2} to 20 eV at $1/K_0 = 0.6$ Vs cm^{-2}. Singly charged precursor ions were excluded with a polygon filter (otof control, Bruker Daltonik GmbH). Precursors for MS/MS were picked at an intensity threshold of 1.500 a.u. and re-sequenced until reaching a 'target value' of 20.000 a.u taking into account a dynamic exclusion of 40 s elution. For DIA analysis, we made use of the correlation of ion mobility (IM) with m/z and synchronized the elution of precursors from each IM scan with the quadrupole isolation window. We used the short-gradient diaPASEF method as described in Meier et al.[80] but performed five consecutive diaPASEF cycles before the next MS1 scan. The collision energy was ramped linearly as a function of the IM from 59 eV at 1/K0 = 1.6 Vs cm^{-2} to 20 eV at 1/K0 = 0.6 Vs cm^{-2}.

QUANTIFICATION AND STATISTICAL ANALYSIS

ClearMap quantification

To quantify microglia distribution in whole brains of mTBI and sham animals, we used ClearMap. As the script was originally developed for quantification of the $cFos^+$ cells, to comply with the offered method, we performed the following pre-processing steps on our microglia data using Fiji before ClearMap:

1. Background equalization to homogenize intensity distribution and appearance of the microglia cells over different regions of the brain, using pseudo-flat-field correction function from Bio-Voxxel toolbox.
2. Convoluted background removal, to remove all particles bigger than relevant cells. This was done with the median option in the Bio-Voxxel toolbox.
3. Two-dimensional median filter to remove remaining noise after background removal. The filter radius was chosen to ensure the removal of all particles smaller than microglia cells.

4. Unshapen mask to amplify the high-frequency components of a signal and increase overall accuracy of the cell detection algorithm of ClearMap.

After pre-processing, ClearMap was applied by following the original publication and considering the threshold levels that we obtained from the pre-processing steps. As soon as the quantification was completed, the data was exported as an Excel file for further analysis.

Deep learning analyses

The segmentation of the stained Aβ plaques represents a key step toward a reliable quantification thereof. We develop a customized, three-dimensional deep learning approach to optimize segmentation of Aβ plaques in the whole brains of 5xFAD animals. Our network architecture is inspired by the well-established U-Net architecture. Our loss function is an equally weighted combination of Dice and binary cross entropy loss. We use the Ranger optimizer, which combines Rectified Adam, gradient centralization and LookAhead. Annotation of our dataset was performed in Fiji and double checked by multiple experts.[81] Our dataset consists of 98 image volumes (300 × 300 × 300 voxel) from one Alzheimer brain; where 34 vol include Aβ plaques, and 64 vol do not contain any plaques. An ensemble of experts including the scientist who imaged the brains labeled all images. We randomly sampled our training set of 85 vol (21 with AD plaques, 64 without AD plaques), our validation set of seven volumes and our separate test set of six volumes. During training and testing we applied suitable data augmentation protocols. In order to assess the quality of our segmentation we calculate a wide range of voxel-wise and Aβ plaque wise segmentation metrics. Based on the reliable segmentation of individual Aβ plaques we continued toward a statistical evaluation of the number and size of Aβ plaques per brain region. First, we registered all of our brains to the Allen brain Atlas, enabling a single voxel assignment to brain structures. For whole brain segmentation we extracted the single connected components using cc3d,[82] which represent our individual segmented Aβ plaques and calculate their total size in voxels as a biomarker. Using this registration and biomarker, we calculated per brain region statistics for the presence and size of Aβ plaques across the whole brain.

Proteomics data processing

Raw files were either searched against the mouse Uniprot databases (UP00000589_10090.fa, UP00000589_10090_additional.fa) or human Uniprot databases (UP000005640_9606.fa, UP000005640_9606_additional.fa). For DDA raw file analysis, we used the MaxQuant version 1.6.7.0 which extracts features from four-dimensional isotope patterns and associated MS/MS spectra. False-discovery rates were controlled at 1% both on peptide spectral match (PSM) and protein level. Peptides with a minimum length of seven amino acids were considered for the search including N-terminal acetylation and methionine oxidation as variable modifications and cysteine carbamidomethylation as fixed modification, while limiting the maximum peptide mass to 4.600 Da. Enzyme specificity was set to trypsin cleaving c-terminal to arginine and lysine. A maximum of two missed cleavages were allowed. Maximum precursor tolerance in the first search and fragment ion mass tolerance were searched as default for TIMS-DDA data. Main search tolerance was set to 20 ppm. The median absolute mass deviation for the dataset was 1.57 ppm for precursors. Peptide identifications by MS/MS were transferred by matching four-dimensional isotope patterns between the runs with a 0.7 min retention-time match window and a 0.05 $1/K_0$ ion mobility window. Label-free quantification was performed with the MaxLFQ algorithm, and a minimum ratio count of 1.[83] For DIA data analysis of the 5xFAD samples isolated from different brain regions, a hybrid library containing all single-shot DIA files and region-specific libraries (16 fractions each) were created using the Spectronaut software suite (version 14.10.201222.47784; Biognosys AG, Schlieren, Switzerland).[84] All files were searched against the mouse Uniprot databases (UP00000589_10090.fa, UP00000589_10090_additional. fa) of canonical and isoform sequences. For DIA single-shot analysis, a minimum of three fragments per peptide, and a maximum of six fragments were included for data extraction. Searches used protein N-terminal acetylation and methionine oxidation as variable modifications. Protein intensities were normalized using the ''Local Normalization'' (Q-value = 0.2) algorithm based on a local regression model.[85] A protein and precursor FDR of 1% was used. Default settings were used for other parameters. Within our regional brain tissue FAD comparison, after filtering and before performing statistical analysis, our data were filtered for at least 3,500 protein identifications per samples and at least 50% data completeness per protein. This resulted in a total of 4,296 protein identifications across 60 samples at a data completeness of above 95%. For downstream analysis, the 5% missing values were imputed from a downshifted normal distribution. For DIA analysis of human heart samples, library free approach was used and the data was analyzed using DIA-NN (Version 1.).[86]

Proteomics downstream data analysis

Proteomics data analysis was performed in the Perseus environment (version 1.6.7.0),[87] Prism (GraphPad Software, version 8.2.1). MaxQuant output tables were filtered for 'Reverse', 'Only identified by site modification', and 'Potential contaminants' before further processing. Protein and peptide identifications were reported after filtering as described above. Proteome correlations across technical/analytical/biological replicates were performed after $\log_{10}$-transformation. Coefficients of variation (CVs) were calculated across the full dataset or within experimental groups on raw intensity levels for shared observations of more than one. Hierarchical clustering was performed in Perseus with default parameters and Pearson correlation as distance parameters. Before DE analysis, data were filtered for at least two observations in one group to be compared, followed by $\log_2$-transformation and imputation from a normal distribution modeled as the dataset with a downshift of 1.8 standard deviations and a width of 0.3 standard deviations. Deep

proteomes of biological replicates from fresh or vDISCO cleared tissue were tested for differences by a two-sided t-test. False-discovery rate control due to multiple hypothesis testing was performed by a permutation-based model and SAM-statistic with an S_0-parameter of 0.2 and an FDR of 0.01. Ontologies for cellular compartment assignment and keywords was performed with the mainAnnot.Mus_musculus.txt.gz followed by log_2-fold difference frequency counts for the terms 'Extracellular space', 'Blood microparticle', 'Neurodegeneration', 'Aging', 'Neurogenesis', 'Receptor', 'Virus-Host', 'Immunity', Wound healing' and 'Cell migration'. 1D enrichment analysis was performed on the two-sided t-test difference and only enriched terms with a size of larger than ten were displayed in the comparison of fresh versus vDISCO deep proteomes. CVs rank plots were calculated within each of the deep proteome groups and plotted against the median abundance of each protein within each group after log_{10}-transformation.

For the calculation of systematic ontology-related protein mass shifts, total protein copy number estimations of the deep fresh and vDISCO cleared proteomes of biological replicates were calculated using the Perseus plugin 'Proteomic ruler'.[88] Protein copy numbers were calculated with the following settings: Averaging mode. 'All columns separately', Molecular masses: 'Molecular weight [kDa]', Scaling mode: 'Histone proteomic ruler', Ploidy: '2', Total cellular protein concentration: '200 g/L'. Proteins were annotated with regards to their cellular compartment by gene ontology from the mainAnnot.mus_musculus.txt.gz. For protein mass estimates, we multiplied the resulting protein copy number by its protein mass for each conditional replicate and summed up all protein masses to obtain the total protein mass for each representative proteome reflecting 100% of the protein mass. To calculate the subcellular protein mass contribution, we calculated the protein mass proportion for the GOCC terms related to the cytoskeleton: 'Actin filament', 'Intermediate filament', 'Centrosome', 'Microtubule'; Membranes: 'Cytoplasm', 'Plasma membrane', 'Membrane'; Organelles: 'Mitochondrion', 'Nucleus', 'ER', 'Golgi apparatus'. For calculating the organellar change between the respective Fresh and vDISCO sub-proteomes, individual protein mass contributions were normalized by its total proteome mass first, followed by ratio calculation to obtain the percentage shift of protein mass between Fresh and vDISCO brains.

For PCA of both LCM applications (mTBI and FAD), data were grouped according to their condition, filtered for at least 760 or 900 proteins for the FAD or mTBI experiment respectively and at least 2 observations within one of the two conditions, column-wise median normalized, and missing values were imputed from a normal distribution with a width of 0.3 standard deviations that was downshifted by 1.8 standard deviations. DE analysis for the FAD and mTBI experiment was performed by two-sided Welch's t-test on LFQ or IBAQ data respectively. False-discovery rate control due to multiple hypothesis testing was performed by a permutation-based model and SAM-statistic with an S_0-parameter of 0 or 0.2 and an FDR of 0.3 or 0.5 for the mTBI and FAD comparison, respectively.

ADDITIONAL RESOURCES

- Videos related to DISCO-MS work: http://discotechnologies.org/DISCO-MS/
- Further details on the vDISCO protocol: http://discotechnologies.org/vDISCO/
- Videos related to workshops: http://discotechnologies.org/workshop/

Supplemental figures

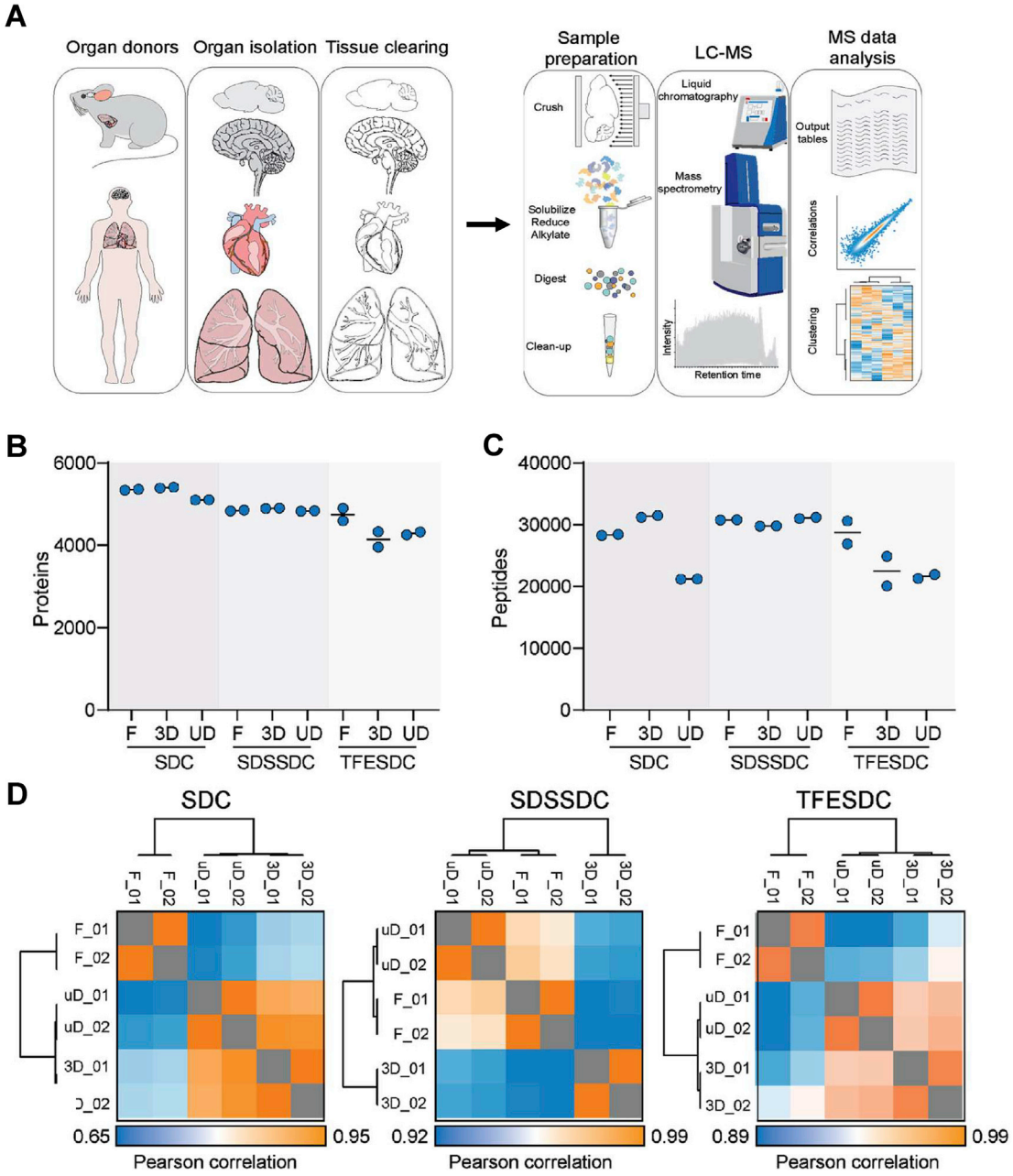

Figure S1. Optimization of sample preparation from cleared tissues, related to Figure 1

(A) The workflow for optimization of DISCO-MS from clearing bulk tissue to mass spectrometry. Organs can be isolated from any organism followed and cleared by any organic solvent-based tissue clearing. The cleared tissues then subjected to sample preparation workflow we developed for the mass spectrometry analysis. In short: the tissues were solubilized, reduced and alkylated, digested into tryptic proteins and cleaned up ready for liquid chromatography coupled to mass spectrometry (LC-MS) analysis. (B) Protein identifications across analytical duplicates for SDC, SDSSDC, or TFESDC preparations coming from fresh or cleared mouse brains (3D, uD: 3DISCO and uDISCO clearing methods, respectively). (C) Peptide levels of the samples shown in (B). (D) Proteome correlation matrices for measurements presented in (B) and (C). High Pearson correlations indicate very similar proteomes across conditions in SDSSDC and TFESDC.

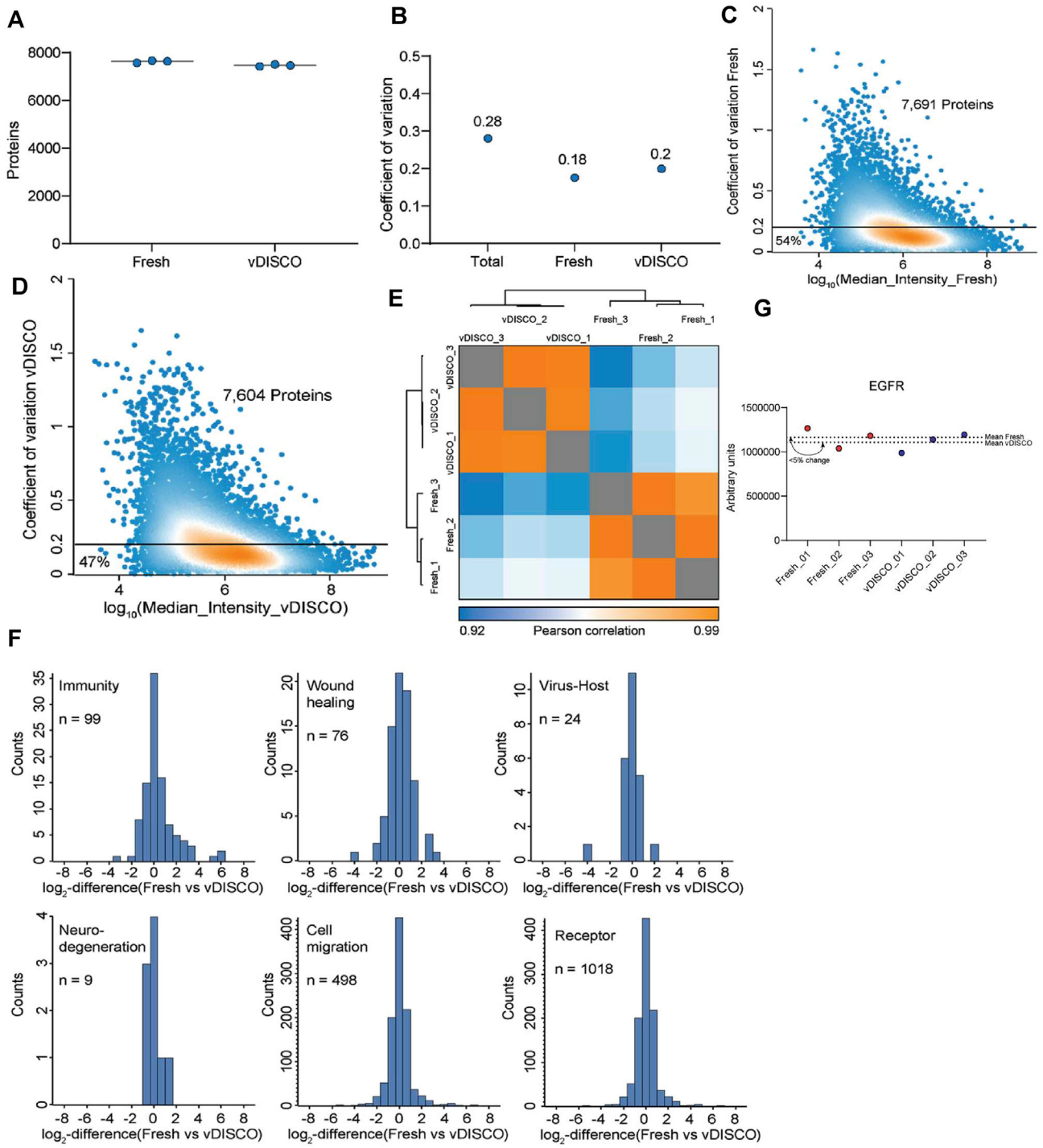

Figure S2. Quantitative assessment of proteome and gene ontologies in vDISCO-cleared and fresh mouse brain tissues in biological triplicates, related to Figure 1

(A) Proteins identified across all three biological replicates for either fresh or vDISCO-cleared tissue. (B) Coefficients of variation (CV) for either the total dataset including fresh and vDISCO cleared tissue, or fresh/vDISCO only. Note that CVs across biological replicates are low and that CVs across biological triplicates are very similar for fresh and for vDISCO highlighting that proteome of vDISCO-cleared organs is highly reproducible. (C) Abundance to CV rank plot for either fresh tissue (left; 7,691 proteins in total; 54% of all proteins are below CV = 0.2) or (D) vDISCO cleared tissue (right; 7,604 proteins in total; 47% of all proteins are below CV = 0.2). (E) Protein intensity correlation plot for all six biological replicates (3x fresh and 3x vDISCO-cleared). (F) Log2-fold changes for the terms 'Immunity' (99 proteins), 'Wound healing' (76 proteins), 'Virus-Host' (24 proteins), 'Neurodegeneration' (9 proteins), 'Cell migration' (498 proteins) and 'Receptor' (1,018 proteins) between fresh and vDISCO-cleared biological triplicates. (G) Mean intensity difference in one of the plasma membrane-associated proteins in fresh and vDISCO cleared brains (N = 3).

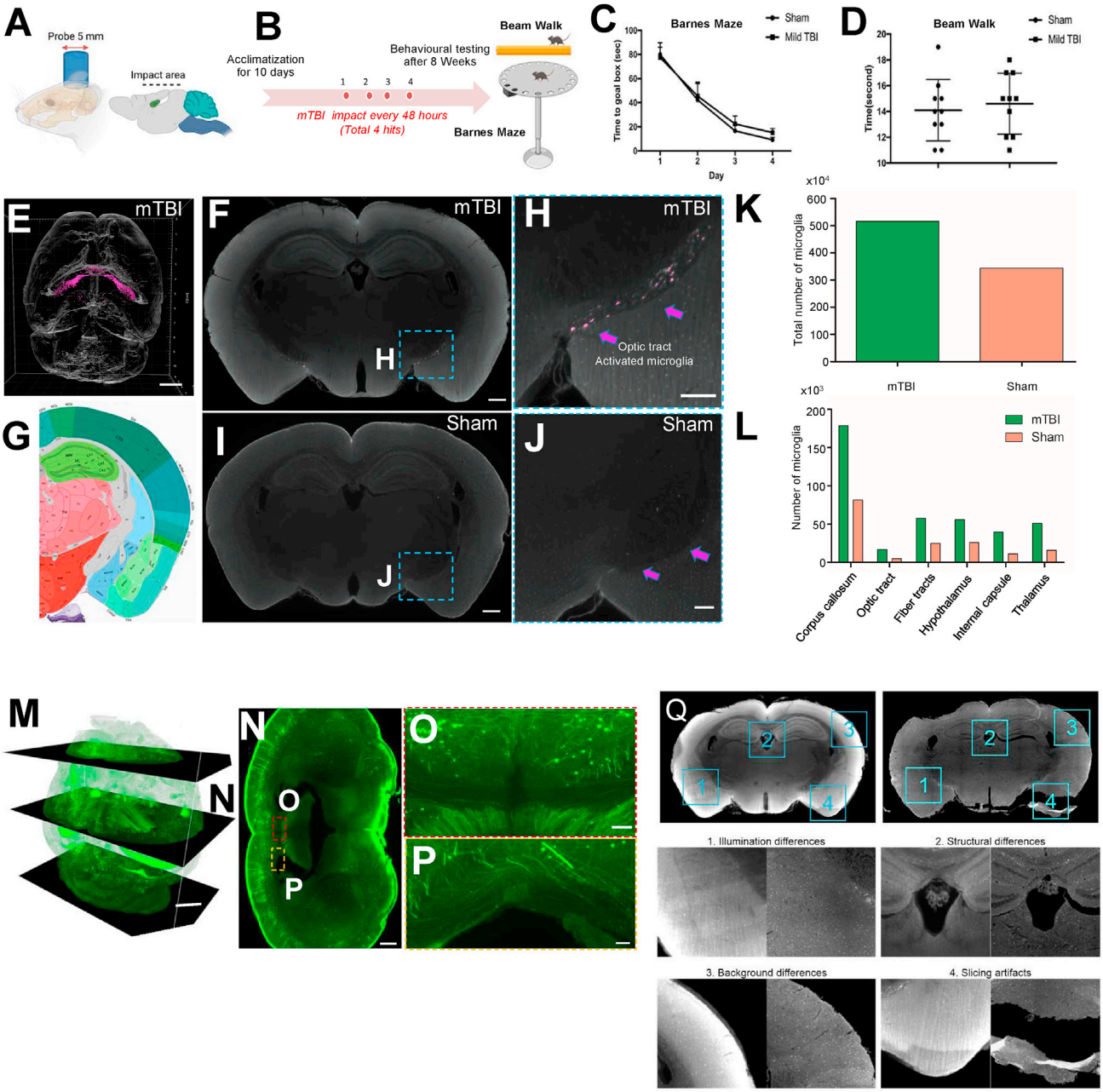

Figure S3. mTBI model validation by behavior and axonal morphology, related to Figure 2

(A) Depicting the mTBI impact area on the intact skull. (B) Schematic plan of the repetitive mTBI experimental mouse model (red points indicate each impact time point). (C) Barnes maze test in sham vs. mTBI animals. n = 10 animals per group. (D) Beam walk test in sham and mTBI animals. n = 10 animals per group. No significant behavior change detected-confirming the "mild" nature of our TBI model. (E) 3D-reconstruction of stiched data of an exemplary CX3CR1GFP+ mouse brain after mTBI. Segmented microglia shown in magenta. Scale bar, 500 μm. (F) Stiched images of coronal optical slices showing optic tract with activated microglia. Scale bar, 400 μm. (G) Corresponding brain regions (coronal view) shown in Allen Brain atlas. (H, J) High magnification image of optic tract in mTBI brain from (F) vs. the same region from sham control brain from (I) showing the activated microglia morphology in mTBI brain compared to control brain. Scale bar, 200 μm, (K) Quantification of total number of microglia in mTBI vs. Sham animals. (L) Quantification of microglia numbers in mTBI vs. sham mice using ClearMap method. Only the regions with major changes are shown. (M) 3D view of stiched images of whole brain from a Thy1-GFP-M mouse after mTBI. Scale bar, 1000 μm. (N) 2D orthoslice of stiched images showing the axonal swellings in corpus callosum (white matter areas). Scale bar, 500 μm. (O, P) High magnification images marked in (N). Scale bar, O, 100 μm and P, 50 μm. (Q) Overview of potential hurdles when registering light-sheet z-planes (left) and LCM sections (right) from the same brain. 1: Light-sheet Illumination can produce striping artifacts and uneven illumination. 2: Small, loosely attached structures such as the choroid plexus inside the ventricles will change shape during slicing. 3: Bulk tissue generates stronger autofluorescence, leading to e.g., uneven background illumination across the cortex. 4: During cryosectioning into 12 μm sections, regions may tear.

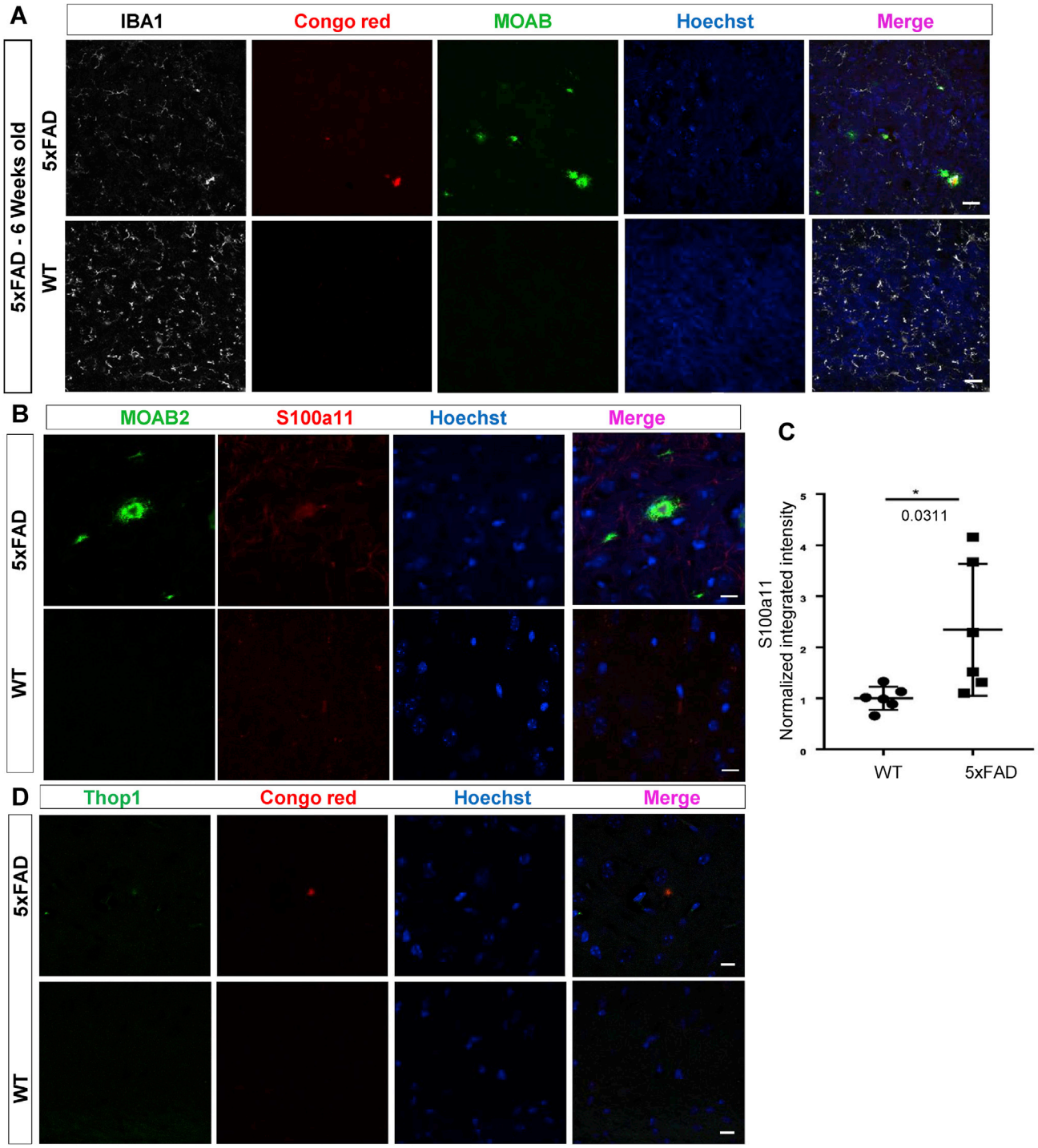

Figure S4. Histological validation of Aβ plaques and DISCO-MS hits in 5xFAD brains, related to Figure 4

(A) Tissue histology validation of Congo red plaque staining with a plaque-specific monoclonal antibody (MOAB, green). Furthermore, the microglia were stained using IBA1 antibody (in white) and nuclei using Hoechst dye (in blue). Microglia activation around the plaques of 5xFAD mouse brain is apparent. Scale bars, 20 μm. (B) Histological validation of DISCO-MS hit S100a11 (red) in hippocampal region using antibody immunostaining in 6 weeks old mice. The plaques were co-labeled using the MOAB2 antibody (in green). (C) Intensity quantification of S100a11 (N = 3 animal per group from total 12 sections; unpaired two-sided Student's *t* test; p = 0.0311; data are presented as average ±SD). (D) Histological validation of DISCO-MS hit Thop1 (in green) in hippocampal region of 5xFAD animals along with Congo red-labeled (in red) plaques in 6-weeks old mice. Scale bars, 10 μm.

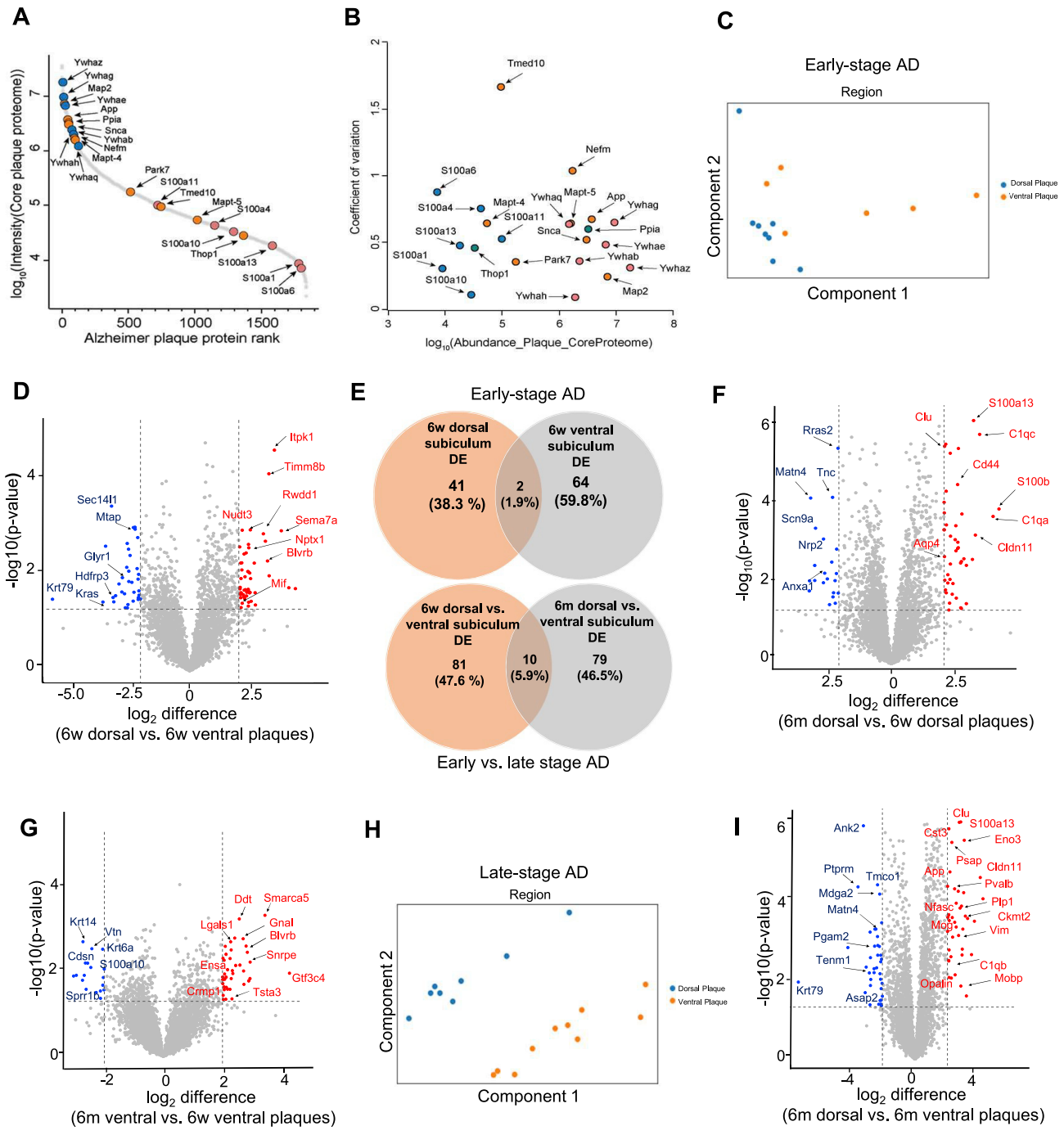

Figure S5. DISCO-MS unravels the spatiotemporally regulated single-plaque proteome in AD mouse model, related to Figure 4

(A) Rank order of core protein signals in a single plaque microenvironment. (B) Log10 abundance distribution of selected proteins and protein families as a function of their coefficient of variation (CV) across the core Aβ plaque proteomes. Dynamic range coverage is up to four orders of magnitude. CVs indicate variability in the shared plaque core proteome, among proteins known to play a role in Alzheimer's disease. (C) Principal component analyses (PCA) in early stage (D) Volcano plot showing the significantly enriched proteins in 6w dorsal vs. 6w ventral plaques. (E) The number of shared and unique set of differentially expressed (DE) proteins in 6w and 6m regions. (F) Volcano plot showing the significantly enriched proteins in 6m dorsal plaque vs. 6w dorsal plaque. (G) In 6m ventral plaque vs. 6w ventral plaque region. (H) PCA in later stage regions. (n = 8–10 ROIs per region). (I) Inter-regional enrichment at later stage plaque.

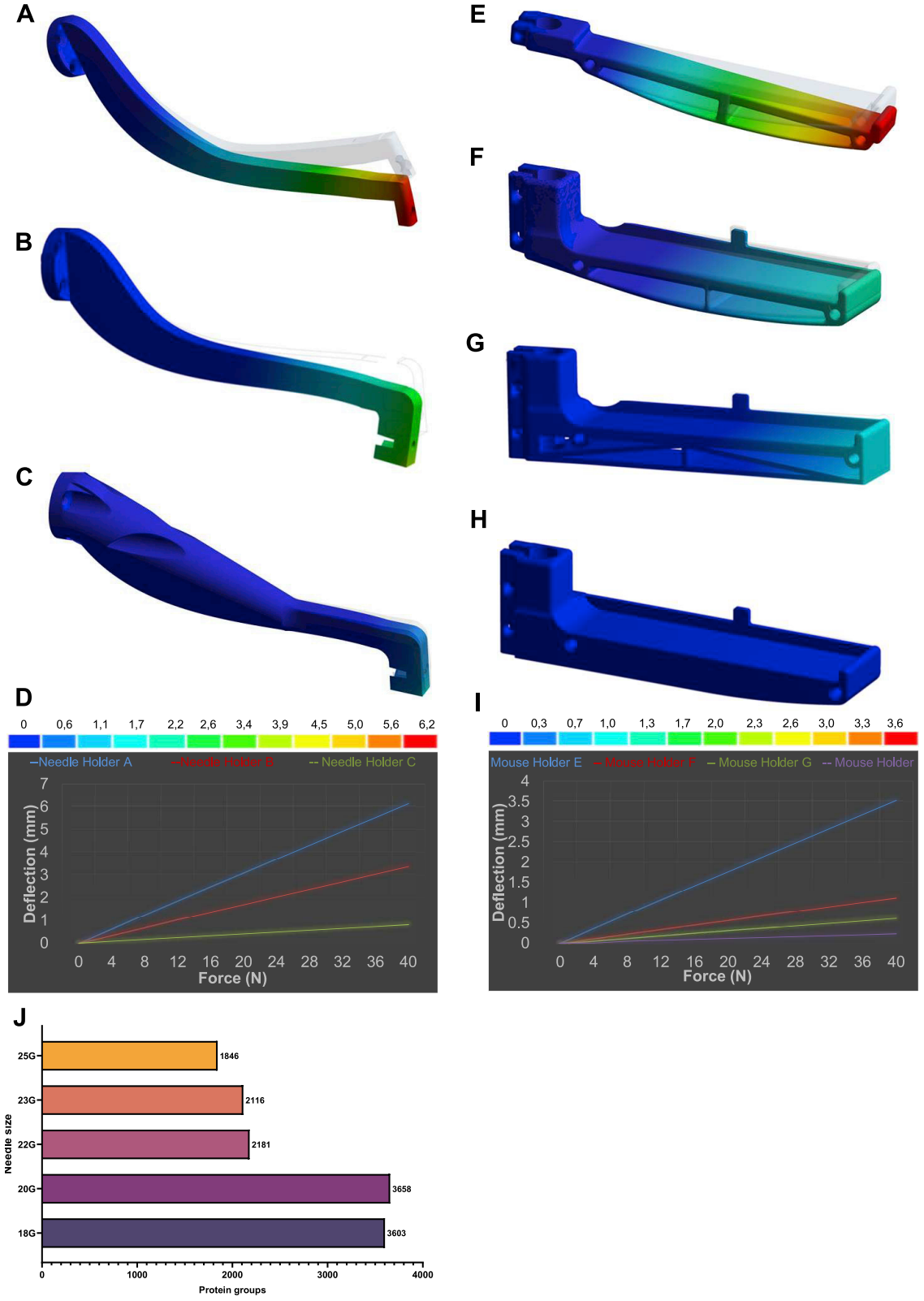

(legend on next page)

Figure S6. Optimization of needle and mouse holders for robotic extraction from whole body, related to Figure 5

(A) The iterative development of the models using finite element analysis method to evaluate the approximate deflection of 6.2 mm for needle holder A, (B) 2.6mm for needle holder B and (C) 0.8 mm for needle holder C. (D) Deflection levels are color coded and plotted to comparatively present the iterative development of the needle holder design. "Images used in A-D courtesy of ANSYS, Inc.". (E) On the other side the maximum deflection levels for the mouse holder (E) is 3.6 mm, for the (F) 1.1 mm, for the (G) is 0.6 mm and for the mouse holder (H) is 0.2 mm. (I) Plot to comparatively present the iterative development of the mouse holder design for the precision of targeting. (J) Showing number of protein groups obtained with various needle gauge size. Note, that in addition to 18G and 22G needles we used here in biological applications (Figures 6 and 7), we could also obtain >1800 proteins with even smaller size needles.

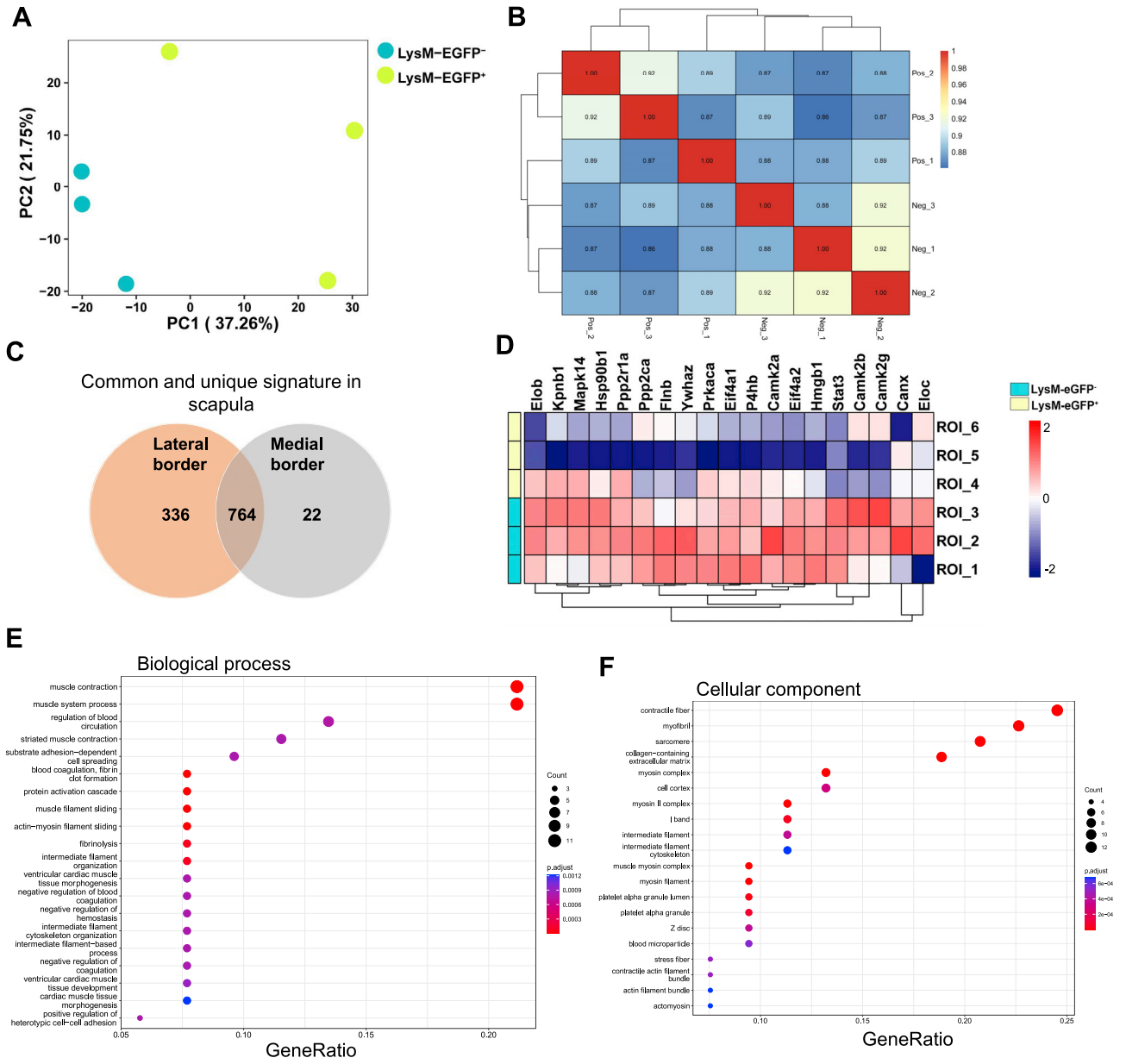

Figure S7. Spatial proteomics from DISCO and SHANEL cleared samples, related to Figures 6 and 7

(A) Principal component analyses (PCA) showing distribution of ROIs in medial and lateral border of scapula bone marrow. (B) Protein intensity correlation plot for all 6 ROIs from LysM-EGFP+ and LysM-EGFP-. (C) Venn diagram showing shared and unique proteins in medial vs. lateral border of mouse scapula. (D) Heatmap showing the proteins related to cytokine pathway in LysM-EGFP+ and LysM-EGFP- scapula samples. (E) Biological process terms associated with regulated proteins in plaques vs. non-plaques regions in human right coronary artery. (F) Cellular component terms associated with regulated proteins.